ENGINEERING

Masticatory system–inspired microneedle theranostic platform for intelligent and precise diabetic management

Jingbo Yang[1,2], Shantao Zheng[2], Deyuan Ma[2], Tao Zhang[1,2], Xinshuo Huang[2], Shuang Huang[2], Hui-jiuan Chen[2], Ji Wang[3], Lelun Jiang[1]*, Xi Xie[1,2]*

Integrated systems for diabetic theranostics present advanced technology to regulate diabetes yet still have critical challenges in terms of accuracy, long-term monitoring, and minimal invasiveness. Inspired by the feature and functions of animal masticatory system, we presented a biomimetic microneedle theranostic platform (MNTP) for intelligent and precise management of diabetes. The MNTP was supported by a miniatured circuit, which used microneedle arrays for on-demand skin penetration, enabling interstitial fluid exudation for simultaneous detection of glucose and physiological ions, and subcutaneous insulin delivery. Interstitial fluid exudation enabled sensing in oxygen-rich environment via the incorporated epidermal sensor functionalized with hybrid carbon nanomaterials. This feature addressed the biosafety issues due to implanted electrodes and the "oxygen-deficit" issues in vivo. The MNTP was demonstrated to accurately detect glucose and ions and deliver insulin to regulate hyperglycemia. The biomimetic and intelligent features of the MNTP endowed it as a highly advanced system for diabetes therapy.

INTRODUCTION

Diabetes is a serious chronic disease characterized by an inability to regulate the blood glucose (BGL), where its complications are the main causes of disability and death (*1*–*3*). The current managements with type 1 or advanced type 2 diabetes are based on frequent detection of BGL through finger-prick blood sampling, which would advise the time and dose of subcutaneous insulin injections (*4*–*6*). In addition, diabetic ketoacidosis is a common diabetic emergency, where the patients often involve potassium and sodium depletion, due to osmotic diuresis, diarrhea, and vomiting (*7*). By analyzing various physiological indicators such as K^+ and Na^+ ions concentration to identify significant hypokalemia or hyponatremia is important for diabetes treatment because inappropriate insulin therapy may decrease serum potassium levels, which theoretically creates a fatal cardiac arrhythmia (*8*–*10*). Clinically, however, the detection of these physiological indicators (BGL and ions) and subcutaneous insulin injections are mainly based on invasive methods with metal needles, which could lead to significant inconvenience and pain on patients, and are prone to the risk of infection (*11*). Although noninvasive sensors including contact lenses (*12*), sweat-based sensors (*13*–*15*), and saliva-based sensors have attracted increasing research interests (*16*, *17*), they are rarely able to reflect glucose levels with clinical accuracies.

Now, continuous glucose monitors (CGMs) are based on subcutaneously implantable glucose electrodes (e.g., Dexcom, Abbott, and Medtronic) to measure glucose concentration in the interstitial fluid (ISF) with Food and Drug Administration–approved accuracy (*18*). Long-term and automatic delivery of insulin is also realized with the development of insulin pump technique (*19*). Promisingly, minimally invasive transdermal technology based on microneedles (MNs) has recently emerged as painless tool for biosensing and drug delivery (*20*). MNs can penetrate the stratum corneum (SC) to create micropores in the skin, where the minimally invasive characteristics of MNs can effectively avoid pain as well as tissue inflammation and fibrosis caused by trauma (*21*, *22*). In particular, MNs have been used for glucose monitoring and insulin delivery (*23*). For example, Voelcker and colleagues (*24*) reported a high-density MN array-based sensing system for the electrochemical detection of glucose in ISF in a pain-free manner, while Yang *et al.* (*25*) presented iontophoresis MN patch (MNP) for the electrically controllable transdermal delivery of insulin. Further, MN-based integration systems for closed-loop diabetic theranostics present advanced technology as artificial pancreas to intelligently regulate diabetes. Gu and colleagues (*26*, *27*) developed glucose-responsive polymetric MNs for regulated release of insulin to treat diabetes. However, the development of closed-loop diabetic theranostic devices still has critical challenges, in terms of sensor accuracy, long-term monitoring, feasibility of electrical device integration, and minimal invasiveness.

The current implantable CGM electrodes, transdermal MN electrodes, and catheters of insulin pump all need to be implanted in subcutaneous tissues for long term, which could cause two main concerns that compromise their applications. First, the implanted materials of electrodes or catheters are prone to induce biosafety concerns by nonspecific adsorption of proteins in vivo, causing local tissue inflammation and fibrosis (*28*, *29*), which could interfere the sensitivity and long-term stability of electrodes in vivo or cause the blockage of catheters of insulin pump. Second, conventional CGM is mainly based on glucose oxidase (Gox) to catalyze glucose oxidation with oxygen in ISF to produce H_2O_2 (*30*–*33*)

[1]Guangdong Provincial Key Laboratory of Sensor Technology and Biomedical Instrument, School of Biomedical Engineering, Sun Yat-Sen University, Shenzhen 518107, China. [2]State Key Laboratory of Optoelectronic Materials and Technologies, Guangdong Province Key Laboratory of Display Material and Technology, School of Electronics and Information Technology, Sun Yat-Sen University, Guangzhou 510006, China. [3]The First Affiliated Hospital of Sun Yat-Sen University, Sun Yat-Sen University, Guangzhou 510006, China.
*Corresponding author. Email: xiexi27@mail.sysu.edu.cn (X.X.); jianglel@mail.sysu.edu.cn (L.J.)

yet generally suffers from "oxygen-deficit" issue in the interstitial space, which causes limited linear detection range in vivo (*34*). An outer membrane could coat an electrode to tune the concentration of glucose to oxygen concentration at the enzyme layer but tends to reduce the electrode sensitivity, which would especially affect MN electrodes with ultrasmall surface area (*35*, *36*). CGM based on the second-generation glucose electrodes used special electron mediators (e.g., wired enzyme) to address the issue of "oxygen-deficit" (*37*), yet it is more challenging and complicated to maintain the stability of these specialized electron mediators in vivo.

Biomimetics of the body functional systems have boosted many creative technologies, such as electronic eyes and cochlear implant, inspired by the animal masticatory system consisting of masseter muscle, teeth, tongue, and oral mucosa that could fulfill the functions of tissue penetration, taste sensing, and saliva secretion. Here, we presented a highly integrated and nonimplanting MN theranostic platform (MNTP) for simultaneous measurement and regulation of diabetes in a closed-loop manner. The biomimetic MNTP used MN arrays for on-demand puncture of the SC layer painlessly, enabling ISF exudation to the MN-integrated epidermal sensor arrays for simultaneous detection of glucose and ions and allowing insulin delivery for diabetic regulation. The biosafety and stability issue of implanted electrodes could be effectively avoided because the MNs were controllably pressed into skin and then instantaneously withdrawn without long-term implantation. Moreover, the ISF exudation feature enabled sensing in oxygen-rich environment via epidermal sensor patch functionalized with hybrid carbon nanomaterials as electron mediator, addressing the challenge of limited electrode surface area and "oxygen-deficit" issues in vivo. The MN-based sensor and drug delivery device were integrated with miniatured circuits, which could mechanically control the automatic pressing of MNs and drug delivery through integrated peristaltic pumps, forming a highly intelligent and closed-loop system. The MNTP was demonstrated to accurately detect glucose and ions and deliver insulin to regulate hyperglycemia, which enabled systematical and long-term monitoring of glucose fluctuations and on-demand therapy in diabetic rat models. The biomimetic, smart, nonimplanting, and closed-loop features of the MNTP endowed this system as a highly advanced system for facilitating diabetic treatments and improving human health.

RESULTS

System design and mechanism

As shown in Fig. 1A, the masticatory system of omnivorous or carnivorous animals (e.g., primates, bears, and canines) consists of masseter muscles, teeth, tongue, and oral mucosa, with diverse functions including tissue penetration, chemical sensing, and molecular delivery. These animals use masseter muscles to drive sharp teeth to bite through the outer layer of food, inducing the interaction between internal substances of food with the oral environment. Animals have taste buds on the tongue surface, which are sensitive receptors that can respond specifically to ions or molecules in food (e.g., sodium ions, potassium ions, glucose, etc.) and generate neurosensory signals. Thus, by biting through the outer layer of food, the tongue senses the chemicals within the exudated tissue fluid of the food. On the basis of the detected taste information of the food, the tongue can produce a feedback response that triggers the secretion of saliva rich with a variety of functional enzymes from salivary glands in the mouth. The saliva enters the tissue and moistens the food or breaks down the food or inhibits bacteria through the enzymes in saliva. The multifunctional integration of tissue penetration, chemical sensing, and molecular delivery in the masticatory system is instructive for the design of closed-loop regulatory devices to interact with subcutaneous space. Inspired by the animal masticatory system (masseter muscle + teeth + tongue + oral mucosa), we designed a closed-loop theranostic system for automatic pressing, skin penetration, glucose/ion sensing, and insulin delivery. A circuit-connected pressing belt is designed to drive the MN array to penetrate the SC, simulating the process of sharp teeth driven by masseter muscles to penetrate the outer layer of food. When the MN array is withdrawn from the skin, subcutaneous ISF can exude along the micropores in the skin punctured by the MNs. To mimic the function of the tongue to sense chemicals, we construct a planar multielectrode array that can sensitively detect glucose, sodium ions, and potassium ions in the exudated ISF, underneath the MN array. On the other hand, to mimic the oral mucosa and salivary glands, we built a drug storage layer connected to a peristaltic pump underneath the MN array, which can be triggered to deliver insulin solution into the subcutaneous space through the MN-induced micropores in skin. The MN sensors and MN delivery device are connected and controlled by an intelligent circuit that mimics the neuromodulatory system of taste perception and feedback saliva secretion. Through the biomimetic design of the masticatory system, this MN theranostic system coordinates the integrated functions of tissue penetration, chemical sensing, and drug delivery.

The conceptual schematic of the biomimetic MNTP was shown in Fig. 1B, where the system was designed to be portable and wearable on a human arm. The MNTP can in situ monitor three physiological analytes including glucose, K^+, and Na^+ and trigger insulin delivery upon the receiving of detection feedback. The MNTP consisted of five components, including an MN puncher @ hybrid electrodes (MNPHE) sensor (mimicking the teeth and tongue), an MN puncher @ delivery patch (MNPDP) device (mimicking the teeth and oral mucosal), an electrically controllable pressing belt (mimicking the masseter muscles), a miniature peristaltic pump (mimicking the salivary glands), and a self-developed printed circuit board (PCB) for signal acquisition and control (mimicking the neuromodulatory system). In specific, MNPHE sensor is mainly composed of seven components, as illustrated in Fig. 1C: (i) a buffering layer to reduce the pressure exerted on the hybrid electrode array; (ii) a hybrid electrode array on a flexible through-holes substrate, for simultaneous detection of three types of analytes (glucose, K^+, and Na^+) from exudating ISF; (iii) a porous sponge for absorbing the ISF and buffering the mechanical deformation of electrode array by MNs; (iv) an MN array for piercing the SC through the through-holes in the electrode substrate, which created microchannels in skin for ISF exudation; (v) an elastic gasket as solution chamber; (vi) medical tape for fixing the sensor on curved skin; and (vii) a polydimethylsiloxane (PDMS) button for transmitting mechanical pressing and rebounding on MNs from pressing belt. The detailed parameters of the components are listed in figs. S1 to S3. The hybrid electrode array was prepared by fabrication processes including laser drilling, metal sputtering, nanomaterials functionalization, and electrode micromachining. First, the flexible polyethylene terephthalate (PET) film, as the substrate of the hybrid electrode, was

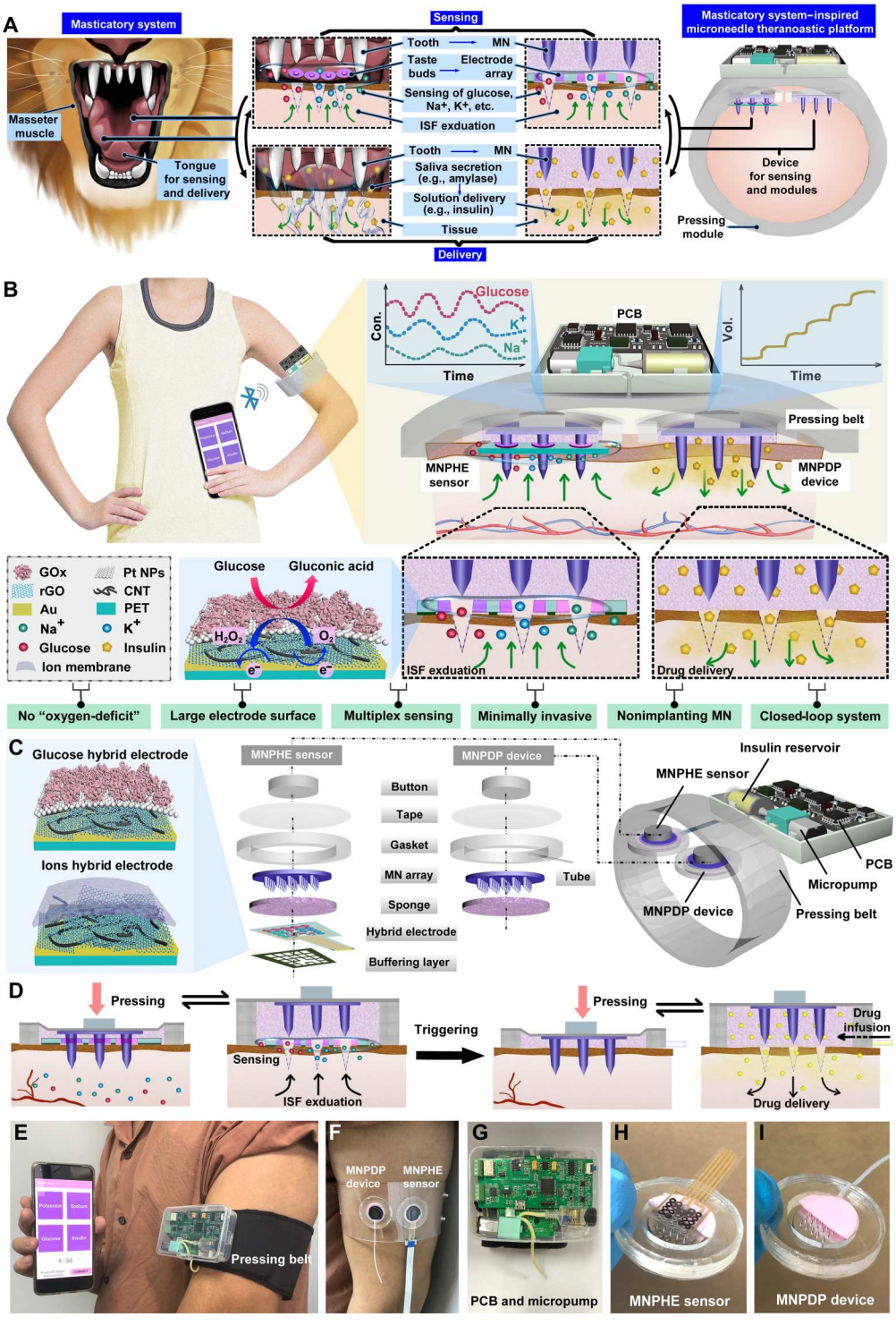

Fig. 1. Schematic drawings and corresponding images of the MNTP. (**A**) Schematic showing the biomimetic design of animal masticatory system. (**B**) Illustration of the MN-mediated MNTP for intelligent and precise diabetic management. The MNTP consisted of an MNPHE sensor, an MNPDP device, an electrically controllable pressing belt, a miniature peristaltic pump, and a PCB. (**C**) Detailed components of the MNPHE sensor and the MNPDP device, as well as the structure of hybrid electrodes functionalized with carbon nanomaterials as electron mediator. (**D**) Illustration of the transdermal sensing and drug delivery strategies of MNTP. The MNPHE sensor followed a mechanism of "MN puncture by pressing & rebounding, ISF exudation, and analytes detection." The MNPDP device followed a mechanism of "MN puncture by pressing & rebounding, insulin pumping and diffusion." (**E**) Photographic image showing the concept of MNTP worn on human arm and wireless communication with smartphone for data transmission and display. (**F**) Digital photos of an MNPHE sensor and MNPDP device worn on arm, fixed by a transparent belt instead of the pressing belt. (**G**) Photographs of the supporting system of PCB-integrated micropump and insulin reservoir. (**H**) Photographs of the MNPHE sensor and (**I**) MNPDP device (the sponges were cut in half to show the cross section).

perforated by laser in accordance with the size and arrangement of MNs, so that MNs could penetrate into the skin through these holes when pressed. Then, the electrode was patterned by Au layer and further modified with different hybrid nanocomposites of reduced graphene oxide (rGO) embedded in carbon nanotube (CNT) network, to improve the electrochemical sensing performance. The rGO and CNT are versatile materials in the field of microelectronics and nanoelectronics, which has abundant chemical groups and defects with high electrochemical activity (*30*, *38*, *39*) due to its superior charge transport properties, large surface area for interaction with biomolecules, and good biocompatibility, and its hybrid nanomaterials have also contributed into advanced electrochemical electrodes with higher sensitivity and responsiveness (*40*, *41*). Here, we modified CNT-rGO nanocomposites as electron

mediators on the electrode surface, where the rGO was tightly embedded into the CNT network to enhance the electrode conductivity. In addition, the dense nanonetwork morphology of CNT was beneficial to increase the pressure-bearing capacity of the electrode and upon pressing. Thereafter, the hybrid electrode was further modified with different sensing components according to the specific functions. For glucose sensing, the standard amperometric method was used. The CNT-rGO electrode surface was electrodeposited with Pt nanoparticles (Pt NPs), which exhibited good electrocatalytic properties for H_2O_2 and were conducive to electron transfer (*42*). Gox was immobilized on the electrode surface by cross-linking of the bovine serum albumin (BSA) and glutaraldehyde mixture. Under a certain voltage, the glucose and oxygen could be catalyzed by the flavin adenin dinucleotide active center of the Gox to produce the gluconic acid and H_2O_2, transferring the electron on the electrode surface and generating a current signal in response to the concentration of glucose. The electron would travel to the Au electrode either through the CNT-rGO electron mediator or through the H_2O_2 that carried the redox electron. For ion sensing, K^+- and Na^+-selective membranes were modified on the corresponding electrode surface using a dip-coating method to form the uniform and specific adsorptive layers. These ion membranes selectively allow the transmission of target ions, thus creating a concentration difference between the inside and outside of the membranes and generating a voltage signal associated with the ion concentration.

The MNPDP device also includes six parts: (i) a porous sponge used as the drug reservoir for storing insulin pumped out of the peristaltic pump; (ii) a flexible microtubing interconnected with the gasket for transporting insulin from the peristaltic pump to the sponge; (iii) an MN array for piercing the SC, which created microchannels in skin for insulin permeation and diffusion; (iv) an elastic gasket; (v) tape, and (vi) a PDMS button same with the above MNPHE sensor. More specifically, the microtubing was connected with peristaltic pumps, which could provide controllable insulin release by appropriate frequency and different duty cycle pulse-width modulation (PWM) waveform. The transdermal sensing and drug delivery strategies of MNTP are illustrated in Fig. 1D. The MNPHE sensor follows a mechanism of "MN puncture by pressing, rebounding, ISF exudation, and analytes detection". The PCB produced electrical signals with certain frequency, which triggers air inflation in the pressing belt to press against the skin. Then, the MN array was protruded through the sponge and electrode substrate to pierce the skin. After MN insertion, the PCB produced electrical signals for air deflation in the pressing belt to reversibly withdraw MNs into the sponge. The MNs created micropores in skin, which allowed the exudation of ISF. The ISF could seep to the hybrid electrode array bypassing the through-holes, due to the pressure difference and suction effect of sponge on top. Moreover, an extra coil motor that control the withdrawing of MN tips could be incorporated to facilitate the ISF exudation during the state of belt pressing (fig. S4).

Glucose and ion concentrations in ISF were measured with the hybrid electrochemical sensor array, where real-time detected signals would be transmitted wirelessly from the MNPHE sensor to a smartphone device via Bluetooth module of PCB. The MNPDP device follows a mechanism of "MN puncture by pressing, rebounding, insulin pumping, and diffusion." Similarly, the PCB triggered the pressing belt to press MN into skin and then retract. The MNs created microchannels in skin, which connected the drug reservoir with subcutaneous space. Dependent on the detected glucose level and the needs of hyperglycemia control, the PCB could trigger the peristaltic pump to infuse insulin into the drug reservoir, which further entered the skin through MN-created microchannels. MNPDP device connected with the micropump can provide accurate drug release by precisely controlling the delivery rate of drug solutions. The sensing and delivery could be repeatedly performed for multiple cycles during a day dependent on the triggering signals.

The whole system with compact size and light weight enables the daily wear by patients without interfering their normal lifestyle habits. Besides, patients can manage their diabetes themselves and catch the real-time sensing results via a smartphone, avoiding the need of care from medical staffs (Fig. 1, E to I). Key advantages of MNTP include the following (Fig. 1B): (i) The hybrid electrode of MNTP has a larger response area than the traditional implantable electrode, which greatly improves sensing accuracy, sensitivity, and mechanical stability. (ii) The "oxygen-deficit" problem of implantable sensors was solved because of the ISF exudation feature caused by MN insertion, which allows sensing in oxygen-rich environment and breaks the limitation of the linear range of glucose detection. (iii) The sensors can realize multiplexed in situ ISF analysis, which simultaneously and selectively measure glucose and ions. Thus, it provides a broader range of disease indicators and references, significantly facilitating the understanding of an individual's physiological state. (iv) MNs can penetrate the SC and create pathways for ISF exudation and insulin transportation, without injuring the subcutaneous tissues and nerves. Thus, MNTP provides better compliance and minimal invasion for diabetic patients compared with traditional implantable CGM electrodes, transdermal MN electrodes, and insulin pump. (v) Nonimplanting MNTP addresses the safety concerns of traditional implantable electrodes, such as in vivo material toxicity and tissue inflammation caused by long-term monitoring. (vi) As a fully closed-loop diabetic management platform, it realizes on-demand insulin delivery based on the direct feedback of detected physiological signals by highly intelligent control algorithm and electronic components.

Performance and characterization of MN penetration

The MN array of this MNTP was fabricated by micromilling technology on stainless steel substrate, where the MNs had ultrahigh stiffness that was desirable for effective skin penetration (Fig. 2A). The structure and morphology of the as-fabricated MNs were characterized by optical microscopy, scanning electron microscopy (SEM), and an ultradepth three-dimensional (3D) microscope (Fig. 2, B to D). Each MN consisted of a cone tip (~15 μm in diameter) and a base with diameter of 480 μm. The MNs were neatly arranged into a 5 × 5 square array with the center distance of 1500 μm. The MN length was 1200 μm, where the exposed length into skin is roughly about 350 μm, considering the presence of compressed sponge and electrode substrate. The mechanical performance of MN array on penetrating skin played an important role in applications, and thus, the mechanical behavior of porcine skin penetration by MNs under compressive loads was investigated (fig. S5). In the "press stage," the resistance force gradually increased with the compression loads on the MN array (Fig. 2E). Once the resistance force reached the rupture limit, the MN array pierced into the skin, corresponding to a drop at point "P." The critical penetration force and

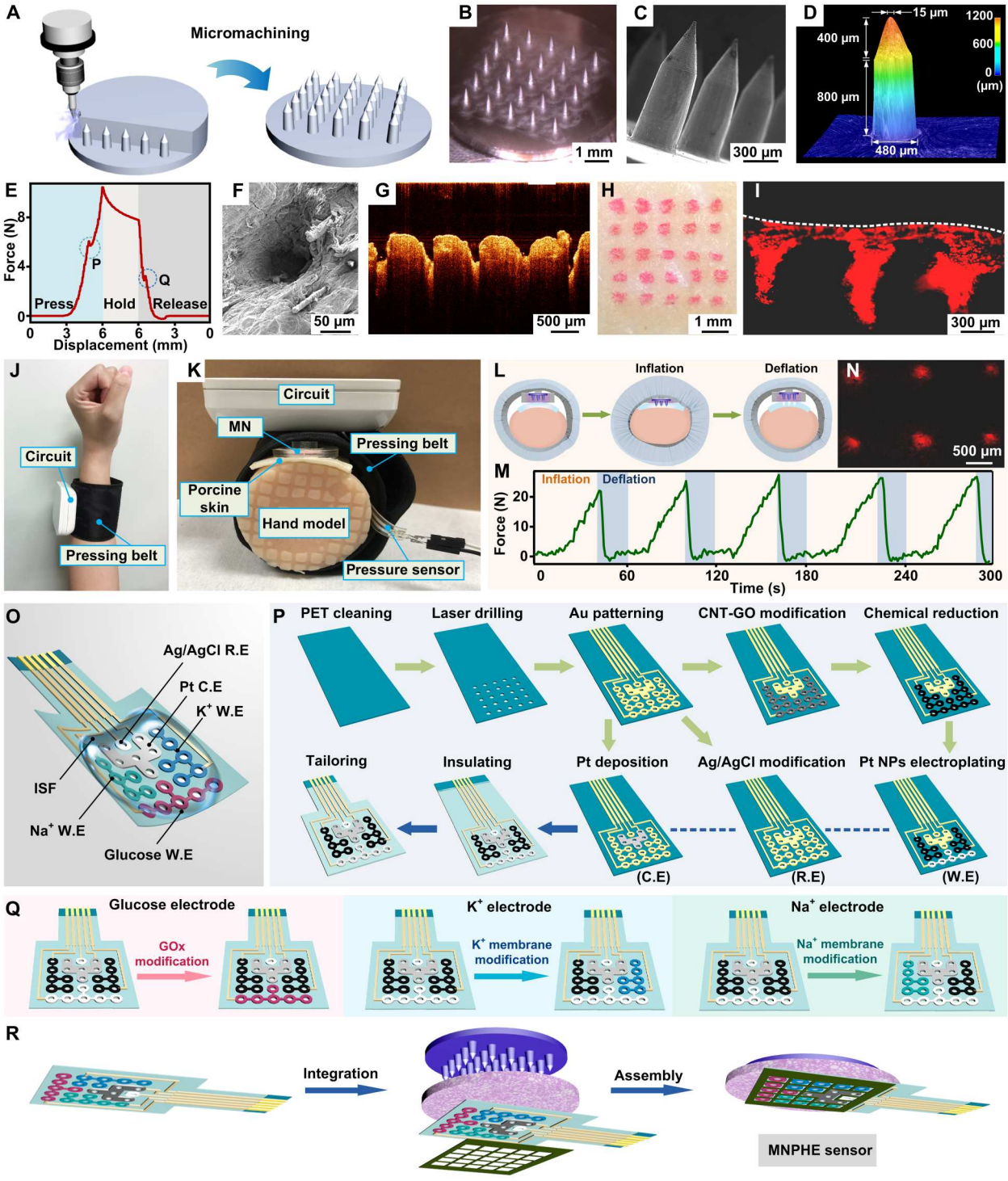

Fig. 2. Characterizations of MNTP and the fabrication of MNPHE sensors. (**A**) Schematic of the MN array fabrication. (**B**) Digital photograph, (**C**) SEM image, and (**D**) 3D reconstruction image showing the morphology of MN array. (**E**) Mechanical curve of the MN array during the "press and release" test. (**F**) SEM image and (**G**) OCT image of the punctured porcine skin by the MN array during the "Pressing and Release" test. (**H**) Top view and (**I**) cross-sectional view of porcine skin tissue after MN penetration. (**J**) Application scenario where the automatic pressing belt induces MN penetration into skin. (**K**) Simulation setup for monitoring the dynamic pressure of the pressing belt during test. (**L**) Schematic of test cycles including 40-s inflation for MN pressing and 20-s deflation for MN retraction. (**M**) Force-time periodic curve of the pressing belt during the "inflation and deflation" test. (**N**) Fluorescence image of the punctured porcine skin by the pressing belt-induced MN insertion. (**O**) Schematic of the hybrid electrode array for multiplexed ISF analysis. (**P**) Fabrication schematic of hybrid electrode array. (**Q**) Preparation of the glucose electrode, K^+ electrode, and Na^+ electrode. (**R**) Schematic showing the integration of MN array with the hybrid electrode array to obtain the MNPHE sensor.

energy were determined to be 6.1 N and 30.2 mJ, respectively. In the "release stage," the measured force gradually decreased with the release of compression on the MN array. Once the MNs were detached from the skin, the friction decreased to 0 N, corresponding to an increase at point "Q." Last, the MN array was completely retracted into the medical sponge, with the corresponding micropores remaining in the skin. After the MN insertion, the micropores in the porcine skin could be clearly observed by the SEM (Fig. 2F) and optical coherence tomography (OCT) (Fig. 2G). The average depth and base width of the poked micropores were ~350 and ~150 μm, respectively, verifying successful skin penetration by the MN array. The observed maximum penetration depth was shorter than the length of MNs (1200 μm), which was likely attributed to the presence of a sponge buffering the insertion of MN tips. To demonstrate drug diffusion after MN penetration, we filled the MNPDP with red fluorescent dye (rhodamine B), followed by observation of fluorescence dye deposition into skin. After the MNPDP was pressed against porcine skin and then withdrawn for 10 min, red fluorescent spots with similar arrangement to MNs were observed on the skin surface (Fig. 2H). The resulting fluorescence distribution around the transdermal zones in skin tissue is examined. Permeation of red fluorescent dye into the subcutaneous tissues through MN-induced microchannels was clearly observed, with a dye diffusion depth of ~850 μm (Fig. 2I and fig. S6). Transepidermal water loss measurement was also used to evaluate the skin recovery time after MN penetration, where the results showed that the skin barrier returned to its normal state in the time scale of 30 min after MN removal (fig. S7).

To simulate the application scenarios where the automatic pressing belt induces MN penetration into skin (Fig. 2J), a circuit-supported pressing belt integrated with MN device was worn on a silica gel hand model, where a pressure sensor is embedded to monitor the dynamic pressure during tests. Upon activation of the pressing belt by the circuit, the belt would drive the MN to penetrate a layer of porcine skin placed between the MN and the gel hand (Fig. 2K). After five cycles of tests (each cycle included 40-s inflation for MN pressing and 20-s deflation for MN retraction) (Fig. 2L), the force-time curves showed a regular periodicity. As inflation time of the belt increased, the pressure force exerted on the arm gradually rose until it reaches the maximum force at 40 s of inflation (Fig. 2M). When deflation began, the pressure force instantly decreased to ~0 N. Because of the recovery of tissue deformation, the force continued to fluctuate smoothly for a period of time. The average of maximum force is 25.34 N, which is much larger than the penetration force of MN array (~6.1 N). Besides, the treated porcine skin was observed, where the array-arranged red fluorescent spots with similar size to MN demonstrated that the MNs indeed created micropores in the skin (Fig. 2N). Thus, both MNPHE sensor and MNPDP device driven by the controllable pressing belt can readily pierce the skin. Because of the on-implanting feature, the electrode patch could be flexibly replaced with a new one during device wearing, to avoid potential electrode instability during long-term application (fig. S8). Moreover, although this MNTP needed repeated insertion of MNs into skin, the insertion position could be readily altered to a different body part on a different day rather than sticking to the exactly same position, to avoid severe damage on the same skin area (fig. S9).

For MNPHE sensor, the ISF would seep from these micropores created by MNs after pressing and then reach the surface of the hybrid electrode, where the glucose, K^+, and Na^+ concentrations could be simultaneously detected. The multiplexed hybrid electrode array had five independent electrodes, including a glucose working electrode (W.E), a K^+ W.E, a Na^+ W.E, a Pt counter electrode (C.E), and a Ag/AgCl reference electrode (R.E) (Fig. 2O). The fabrication process of the hybrid electrodes was illustrated in Fig. 2P. Briefly, through-holes were prepared on a cleaning PET substrate according to the arrangement of MN tips by laser drilling. Next, a thin Cr/Au layer was patterned on the PET substrate following the pattern of metal masks to define the electrode positions. Mixture of CNT and GO was deposited on the W.Es, where GO was further reduced into rGO. The rGO was embedded in the CNT nanomesh, which synergistically served as electrode mediator to facilitate electron shuttle from the functional layers to the Au electrodes. For the glucose electrode, the W.E was coated with Pt NPs via electrodeposition, followed by functionalization with Gox (Fig. 2Q). The solid-contact ion-selective electrodes were coated with either K^+-selective membrane or Na^+-selective membrane, respectively (Fig. 2Q). The C.E was deposited with a Pt layer by magnetron sputtering, while the R.E was coated with Ag/AgCl conductive inks and modified with polyvinyl butyral (PVB). Subsequently, the nonelectrode areas were insulated with PDMS, and the whole electrode patch was tailored according to the device architecture. After these steps, the hybrid electrode array was obtained and would realize simultaneous detection of glucose, K^+, and Na^+. It was then further integrated with the MN array and other components into the MNPHE sensors (Fig. 2R).

Characterization of MNPHE sensors

The surface of the bare Au electrode displayed a smooth profile, while the CNT-GO–modified Au electrode exhibited nanostructural topography with interlaced and fibrous morphology (Fig. 3A), corresponding to the typical features of 1D CNT bridging different CO nanosheets. After the chemical reduction, the CNT-rGO/Au electrode displayed a slightly altered profile compared to the original CNT-GO–modified electrode, where the 2D rGO nanosheets were observed to embed in the CNT network. The surface of the CNT-rGO–modified Au electrodes showed more graphene-like sheet feature with folds and wrinkles in the SEM image. After functionalization with Pt NPs, Pt NPs with the size of <100 nm was homogeneously dispersed on the surface of CNT-rGO nanosheets. To confirm that the GO was successfully reduced to rGO, we analyzed the elements of the hybrid electrode via energy-dispersive x-ray (EDX) (Fig. 3B). Before chemical reduction, the number ratio of C to O atoms in GO was close to 2.3:1, while this ratio increases to 5.6:1 after reduction, suggesting that the GO was successfully reduced to rGO, which contains less O atom ratio. There are oxygen-containing functional groups and defects on rGO due to the incomplete reduction, which serves as the anchoring sites for Pt NPs and as chemically active sites for catalytic reactions. Pt element was detected in EDX as well, consistent with the fact that Pt NPs were generated on the Pt NPs/CNT-rGO hybrid electrode. Optical image of the as-fabricated hybrid electrode array after surface modification was shown in Fig. 3C, where the electrode patch was flexible and bendable. MN array could be integrated with the hybrid electrodes patch according to the positions of the through-holes on the electrode substrate. The electrochemical performance of the glucose hybrid electrode was investigated with cyclic voltammetry (CV), where performance of the Pt NPs/CNT-

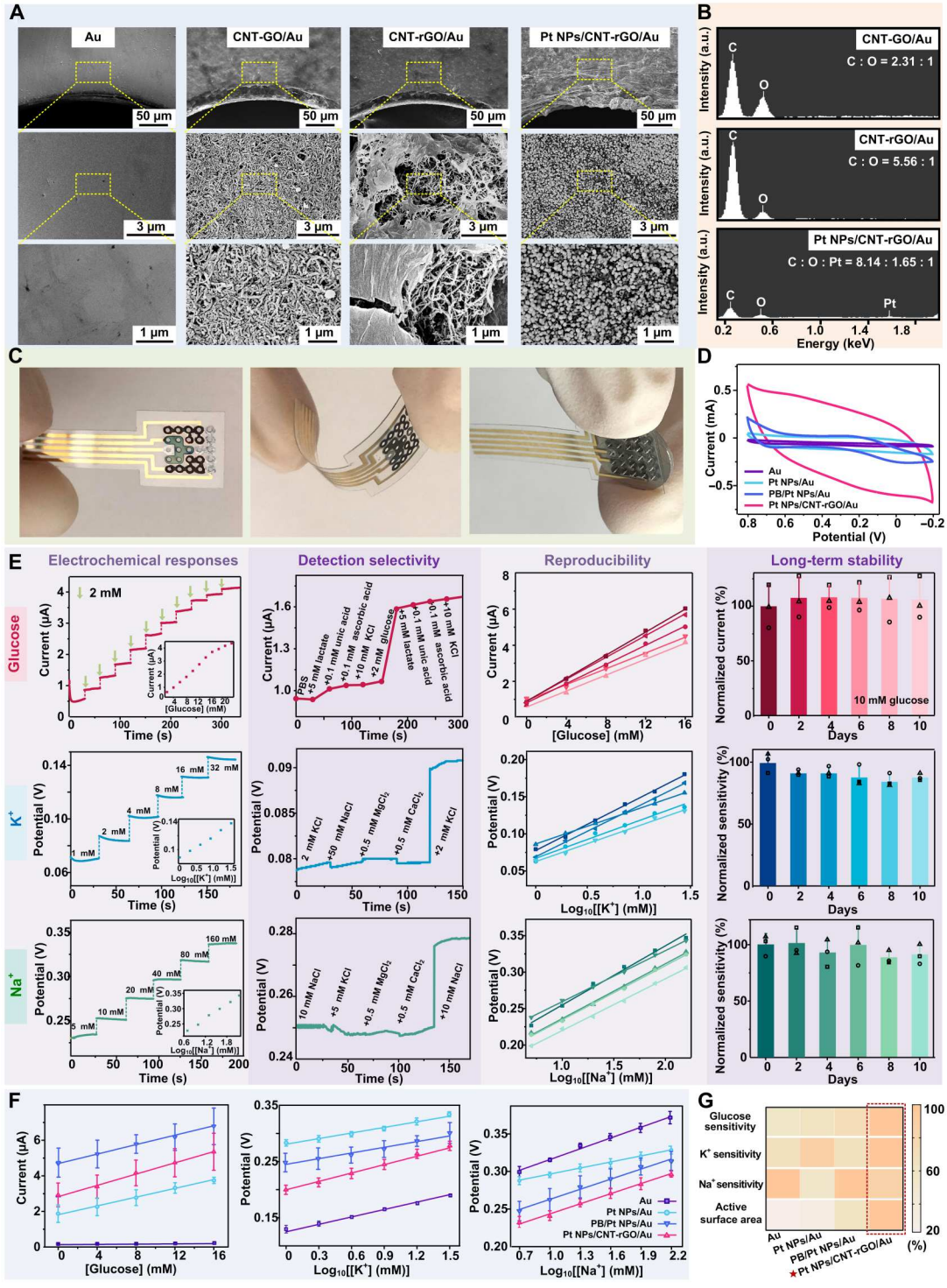

Fig. 3. Electrochemical characterizations of hybrid electrode arrays. (**A**) SEM images with different zoom-in magnifications of the surface morphology of hybrid electrode arrays in different modification stages. (**B**) EDX spectrum of the surface of different electrodes. a.u., arbitrary units. (**C**) Digital photograph of as-fabricated hybrid electrode arrays including a front view (left), the electrode array upon bending (middle), and the electrode array integrated with MN array (right). (**D**) CV curves of different electrodes including Au electrodes, Pt NPs/Au electrodes, PB/Pt NPs/Au electrodes, and Pt NPs/CNT-rGO/Au electrodes (namely hybrid electrodes in this work). (**E**) The detection performance of the hybrid glucose electrode, K^+ hybrid electrode, and the Na^+ hybrid electrode of the MNPHE sensor. The electrochemical responses (amperometric/potentiometric responses), selectivity, reproducibility, and long-term stability were systematically evaluated. (**F**) Amperometric responses of glucose (left), K^+ potentiometric responses (middle), and Na^+ potentiometric responses (right) of different electrodes including Au electrodes, Pt NPs/Au electrodes, PB/Pt NPs/Au electrodes, and Pt NPs/CNT-rGO/Au electrodes. $N = 3$ groups. (**G**) Heatmap plot summarizing the electrochemical performances (glucose detection sensitivity, K^+ detection sensitivity, Na^+ detection sensitivity, and active surface area) of the different types of electrodes.

rGO/Au electrode as W.E was compared with control groups including Au electrodes, Pt NPs/Au electrodes, and Prussian blue (PB)/Pt NPs/Au electrodes. PB was an effective redox mediator that has been widely used for in vitro glucose sensor, although PB was inhibited for applications for in vivo because of its cytotoxicity. Here, our results revealed that the Pt NPs/CNT-rGO/Au electrode exhibited the largest area enclosed by CV curves, compared to the control groups of bare Au electrode, Pt NPs/Au electrode, and even the PB/Pt NPs/Au electrode, suggesting the electrochemical superiority of Pt NPs/CNT-rGO/Au structure (Fig. 3D). These results suggested that the CNT-rGO materials improved the electrochemical performance of the glucose hybrid electrode, likely because of the fact that the CNT-rGO provided extra surface area for

contacting with Gox and extra pathway for electron shuttle from Gox active center to electrode, besides the H_2O_2-mediated pathway.

The performance of glucose hybrid electrode was tested in vitro. For the sensitivity, the measured current intensity increased with the increasing concentration of glucose, which exhibited representative amperometric signals of the electrodes in response to the glucose solutions (Fig. 3E and fig. S10). The amperometric response of glucose electrode displayed two linear ranges, where the first one was fitting the glucose concentration range of 2 to 16 mM with a correlation coefficient of 0.995 and with a typical sensitivity of 0.222 μA/mM. Such detection range covered the normal range of BGL in human blood (approximately 3.6 to 7.5 mM, empty stomach) (*43*). The second linear range of glucose detection was from 16 to 22 mM, with a correlation coefficient of 0.998 and with sensitivity of 0.159 μA/mM (fig. S11). The BGL diagnosed as hyperglycemia in clinical practice is more than 7.0 mM in fasting or exceeds 11.1 mM in 2 hours after meal (*31*). Therefore, the as-fabricated glucose hybrid electrode was qualified to monitor the glucose fluctuation of diabetics. For the selectivity, the minimum and maximum interference signals generated by each interferer were ~9.5 and ~1.6%, respectively (Fig. 3E). The nontarget analytes caused negligible interference to the response of each electrode, which demonstrated a good anti-interference capability of the glucose hybrid electrode. For the reproducibility (Fig. 3E), all amperometric responses increased with the increasing glucose concentration, where linear curves had the relative SD in a sensitivity of ~9.1%. It indicates that the responsiveness of the same functional electrodes obtained under different batches exhibits similar trends and sensitivities. Besides, long-term stability studies were conducted to explore their storage stability. The final relative current of glucose hybrid electrodes in the 2nd, 4th, 6th, 8th, and 10th day is 107. 7 ± 18.9%, 107.9 ± 10.6%, 107.7 ± 13.0%, 106.8 ± 20.5%, and 106.3 ± 19.24%, respectively (Fig. 3E), suggesting that the sensitivities of the glucose hybrid electrodes are consistent over a period of at least 10 days.

For K^+ hybrid electrodes, the sensitivity, selectivity, reproducibility, and long-term stability were also evaluated (Fig. 3E). For the sensitivity, the measured potentiometric signals showed a concentration-dependent out-step upward trend. The K^+ hybrid electrode exhibited a correlation coefficient of 0.997 with the sensitivities of 63 mV per decade of concentration (fig. S11). For the selectivity, the maximum interference signals generated by each interferer were only ~3.6%. The reproducibility was investigated by recording the potentials of five K^+ hybrid electrodes. The linear curves had the relative SD in a sensitivity of ~10.8%. For the long-term stability, final relative sensitivities in the 2nd, 4th, 6th, 8th, and 10th day are 91.6 ± 2.1%, 92.1 ± 4.3%, 88.3 ± 8.5%, 85.1 ± 5.3%, and 87.9 ± 2.9%, respectively. The K^+ hybrid electrodes showed a sufficient stability with slightly decreased sensitivities after 10 days, while this minor sensitivity alternation could be readily addressed by electrode calibration in applications. Similarly, the potentiometric signal demonstrated that Na^+ hybrid electrode had a correlation coefficient of 0.998 with the sensitivities of 59 mV per decade of concentration (fig. S11). In addition, the interference signals generated by each interferer were less than 7.4%. The relative SD of sensitivity among five Na^+ hybrid electrodes is only ~6.5%. Besides, the final relative sensitivity in the 10th day is 91.1 ± 8.8%, which showed excellent stability of Na^+ hybrid electrodes (Fig. 3E).

To examine the electrochemical effects of the nanostructured hybrid electrodes of CNT-rGO material modification, we comprehensively evaluated the glucose detection sensitivity, K^+ detection sensitivity, Na^+ detection sensitivity, and the active surface area by comparison with bare Au electrode, Pt NPs/Au electrode, and PB/Pt NPs/Au electrode. The values of the tested sensitivities (Na^+, K^+, and glucose) and active surface area of different electrodes were normalized and quantitatively compared in a heatmap plot (Fig. 3G) and a histogram plot (fig. S12). The Pt NPs/CNT-rGO/Au electrode exhibited a sensitivity of 0.179 μA/mM for glucose detection, which was almost 45-fold higher than that of Au electrodes, and 1.3-fold or 1.4-fold higher than that of PB/Pt NPs/Au electrode or Pt NPs/Au electrode, respectively (Fig. 3F). This was likely attributed to the elevated electrocatalytic activity by the functionalization with well-dispersed Pt NPs and facilitated electron transfer by the interconnected CNT-rGO nanocomposites due to the higher nanostructural surface area for enzyme contacts. On the other hand, the detection sensitivities of Na^+ and K^+ displayed slight improvement for Pt NPs/CNT-rGO/Au electrode (Fig. 3F) While the ion-selective membranes played a predominant role to maintain stable response potentials in different solutions, the lone-pair electron of rGO defect sites could attract cations and promote the cations bind of ion-selective membrane. The linear range and limit of detection were summarized on fig. S13 and table S2. Overall, the Pt NPs/CNT-rGO/Au hybrid electrodes exhibited optimized detection properties for both glucose and ion sensing and had good biocompatibility without concerns of toxicity existed in other electron mediators such as PB.

Characterization of MNPDP devices

The mechanism of transdermal insulin administration by the MNPDP devices was theoretically simulated via the creeping flow and the transport of diluted species interface in COMSOL Multiphysics. The simulation used a simplified 2D model as illustrated in Fig. 4A and fig. S14, with the geometries and components mimicking the actual setup. The skin was modeled as three layers (SC, epidermis, and dermis) with corresponding mass diffusivities (table S2). The MNPDP was compared with another two groups, the MNP and the topical patches (TPs). In specific, (i) for the MNPDP device, the MN was inserted into the skin and retracted into the reservoir, followed by 1-min pumping and 59 min of drug diffusion; (ii) for the MNP, the MN is inserted into the skin and retracted into the reservoir, without drug infusion by pumping; (iii) for the TP, it provided 60-min passive diffusion on the surface of the intact skin. The temporal diffusion profiles and spatial distribution in tissues of drug delivery by the three devices were systematically explored. The MNPDP gradually mediated drug infiltration into the dermis with a drug infusion rate of 250 μl/min, and a remarkable amount of drug distribution in tissue was observed after 1-hour delivery. In contrast, the MNP without active pumping delivered notably less amount of drug into dermis, while the transdermal delivery mediated by TP failed because of SC barrier (Fig. 4B), which was consistent with the 3D model (fig. S15). More specifically, diffusion amount of insulin administrated with MNPDP device was significantly facilitated by the micropump, which was ~2.7-fold higher than MNP (Fig. 4C). Especially in the initial 1 min, a pulse diffusion flux of insulin could be observed whereby the insulin delivery rate was maximized. It might be explained that the micropump provided greater liquid pressure and impetus to promote

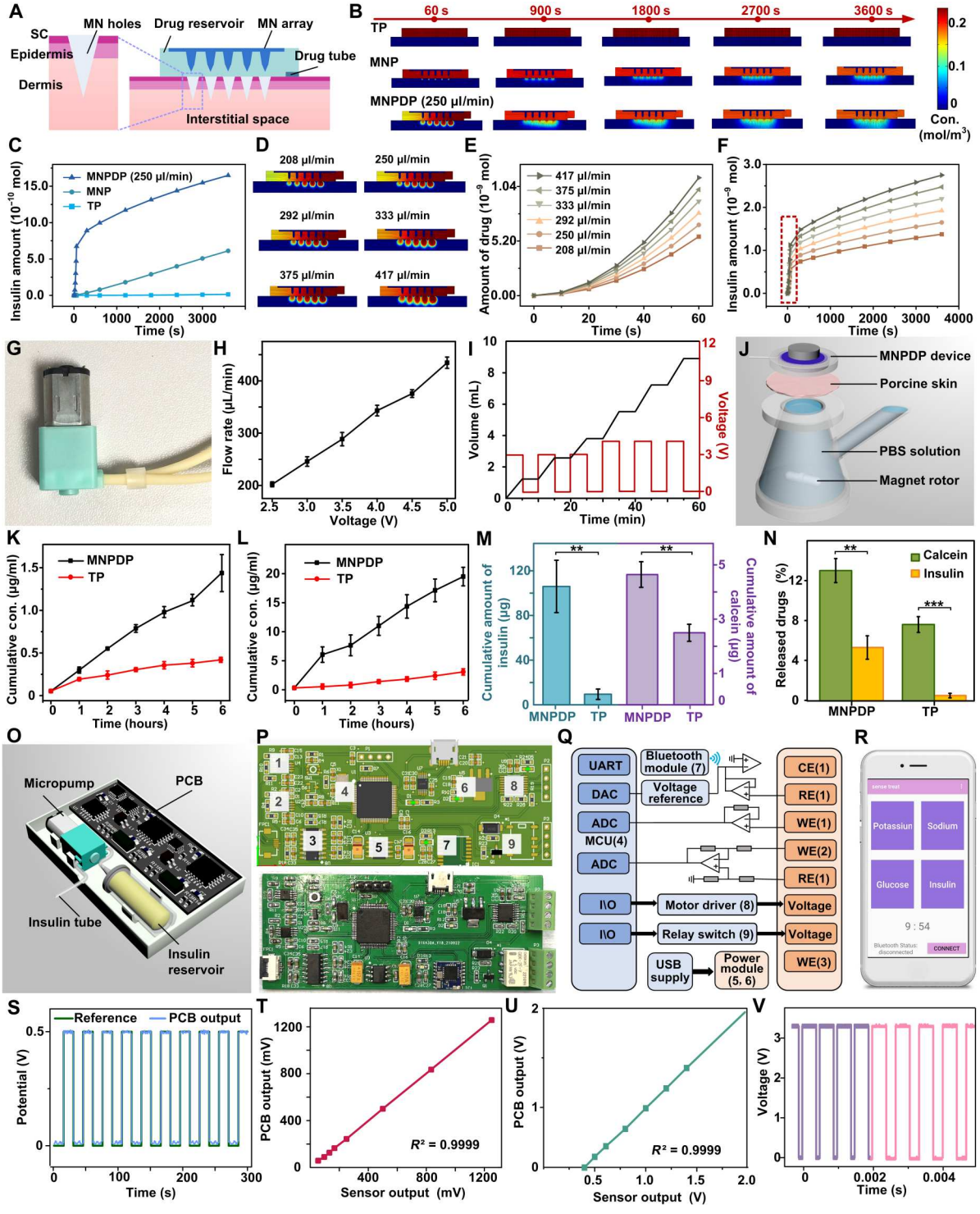

Fig. 4. Characterizations of the MNPDP device and the test of PCB. (**A**) Illustration of the COMSOL model of MNPDP device. (**B**) Insulin concentration distribution and (**C**) total delivered amounts with different methods. (**D**) Insulin concentration distribution and (**E**) delivery amount within the first 1 min using MNPDP with different flow rates. (**F**) Delivery amount of insulin within 1 hour using MNPDP with different flow rates. (**G**) Photograph of the micropump connected with MNPDP. (**H**) Calibration curve of the micropump flow rate as a function of applied voltage. (**I**) Cumulative insulin volume using micropumps subjected to different periodic voltages. (**J**) Illustration of Franz diffusion cells. (**K**) Cumulative calcein and (**L**) insulin concentrations in receptor chamber using TP and MNPDP within 6 hours. (**M**) Cumulative permeation amount and (**N**) percentage of insulin and calcein within the first 1 hour. (**O**) Schematic view of the PCB and its components. (**P**) Design sketch (top) and the photograph of a PCB (bottom). (**Q**) System block diagram of PCB. (**R**) Home page of the smartphone APP. (**S**) The output voltages of PCB at intermittent constant voltages of 0 to 0.5 V. Input-output signal calibration for (**T**) glucose and (**U**) ion sensing signal channels. (**V**) Output voltages of PCB with different duty cycles.

insulin permeation through microholes. Once the micropump stops working, the insulin amount increased slowly like in the MNP model. In addition, as the flow rate of the micropump increased linearly, the accumulated amount of insulin also increased linearly as expected, both in the first 1 min and the total delivery period (Fig. 4, D to F, and figs. S16 and S17). Thus, this MNPDP device could provide an on-demand drug delivery strategy, which combined controllable rapid release and sustained release.

Next, insulin released using MNPDP device in vitro was investigated, which was supported by a micropump to precisely control the infusion of insulin. The micropump (Fig. 4G and fig. S18) was controlled by modulated pulse signals generated via microcontrollers on electrical circuitry. The flow rates could be precisely tuned by the applied voltage of pulse signals, where the work voltage of the micropump in the range of 2.5 to 5 V would result in the flow rates between 202.18 and 434.64 μl/min (Fig. 4H). In addition, when the micropump was programmed to periodically generate pulse signals at 3 V for 3 cycles and at 4 V for another 3 cycles, the delivered insulin dosages changed according to the triggering signals (Fig. 4I). The micropump displayed precise response and delivery, where the pumping process was completely stopped as soon as the applied signal was zeroed, while the delivery was rapidly turned on upon the application of voltage signals. This result demonstrated feasibility of on-demand drug administration and controllable transdermal delivery of MNPDP driven by a micropump. Furthermore, in vitro permeation experiments were conducted by using Franz diffusion cells, which was covered with porcine skin to mimic the transdermal delivery (Fig. 4J). The diffusion process of either insulin (~5.8 kDa, typical macromolecular drug) or calcein (~622.5 Da, modeling a small molecular drug) was performed by both MNPDP and TP. After 6 hours of exposure, an obvious difference in cumulative permeation concentration was clearly observed. The cumulative concentrations of insulin and calcein increased faster in the MNPDP group than in the TP group. According to the standard curves in fig. S19, the insulin concentration using MNPDP was 19.5 ± 1.6 μg/ml during the total 6 hours, while those by TP was only 4.3 ± 0.1 μg/ml (Fig. 4K). The calcein concentrations administrated by MNPDP and TP were 1.5 ± 0.2 and 0.4 ± 0.03 μg/ml, respectively (Fig. 4L). In the first 1-hour delivery, the cumulative amount of insulin using MNPDP (~105.88 μg) was ~11.1 times higher than that in TP group (~9.54 μg). Similarly, the cumulative amount of calcein using MNPDP was increased by ~4.67 times compared with TP (Fig. 4M). The results suggested that MNPDP enabled a more rapid insulin delivery in comparison to the situation without MN. However, the released percent of insulin was lower than of calcein, both in MNPDP and TP groups (Fig. 4N). It could be explained that the release of insulin was likely prevented because of its much larger molecular weight than calcein.

Design and tests of supporting PCB

The PCB module, as a microcontroller (Fig. 4O), incorporated the required integrated circuit chips and peripheral electronics for electrochemical recording, signal processing, control and feedback, drug infusion, and Bluetooth wireless transmission circuitry, thus forming a fully integrated and programmable MNTP system. Figure 4P illustrated the design sketch and the photograph of the flattened PCB, and the detail of each labeled component was discussed in figs. S20 to S28. The MNTP mainly consisted of a five-electrode system, low–power consumption Bluetooth module, power module, motor driver module, and pressing module (Fig. 4Q). A direct voltage signal would be applied to trigger the relay switch for activating the pressing device at programmed intervals (e.g., every 30 min or every 2 hours in our experiments), which drove the MN to penetrate the skin layer. At the same time, the two-electrode system for ion sensing could record the potentiometric signals that reflected ion concentrations in the seeped ISF. The three-electrode system for glucose sensing could output bias potentials and record amperometric signals related to glucose concentrations. The analog signals were transmitted to the microprogrammed control unit (MCU) and converted into digital domains through the digital-to-analog (DAC) port in microcontroller. The data output by MCU would be real-time observed through an onboard wireless transceiver. Once the hyperglycemia state was detected, the motor driver module could control the rotational speed of the peristaltic pump motor, driving infusion of drug solution into the MNPDP device with set flow rates. The smartphone APP (Fig. 4R) displayed the interface and real-time monitoring of analyte data, conceptually demonstrated a fully integrated MNTP-based hardware and software for diabetes management.

The output voltages of PCB were stable at 0 and 0.5 V, highly consistent with the reference value, which was suitable as bias potential for glucose sensing of MNTP (Fig. 4S). The linear accuracy of the acquisition and output signals of the PCB were characterized, where both signal-conditioning channels (three-electrode system and two-electrode system) demonstrated an excellent linear response (correlation factor $R^2 = 1$) (Fig. 4, T and U). Eliminating the nonideal effects such as voltage offset and obtaining exact numerical linearity of output and input were beneficial to the subsequent signal calibration and processing at the software level. MCU could output a 3.3-V duty cycle of different PWM signals to control the drive motor chip (5-V output) and then determine flow rates of the micropump. Thus, the different duty cycles could be equated to different constant voltages. The MCU could continuously output different PWM signals with different duty cycles (80% indicated by purple line and 60% indicated by pink line), corresponding to 4- and 3-V output of the driver chip (Fig. 4V). Thus, the micropump can be achieved with exact controllability of the electrified time and flow rates.

Performance characterization of MNTP in vivo

In situ ISF monitor via MNPHE sensor and on-demand drug delivery via MNPDP device were examined in vivo. The hair on the back of Sprague-Dawley rats was shaven, then both MNPHE sensor and MNPDP device were fixed on the back, and the MN could penetrate the SC of rats upon pressing (Fig. 5A). In the first set of experiment, the detection of three analytes (glucose, K^+, and Na^+) in ISF with the MNPHE sensor was assessed on healthy rats (three rats in parallel) every 30 min, lasting for a total of 4 hours. The output signals of the three analytes from the hybrid electrode were recorded and converted to concentration of analytes according to the standard curve of MNPHE sensor. The rats were injected intraperitoneally with glucose solution at time points $t = 30$ min and $t = 120$ min (indicated by black arrows in Fig. 5B), to induce fluctuation of glucose levels in vivo for sensor evaluation. To examine the detection accuracy of the MNPHE sensor, the glucose, K^+, and Na^+ in the blood of rats were also measured using a commercial glucometer or a biochemical analyzer as references. Considering the difference between in vivo and in vitro environment, the detection results in

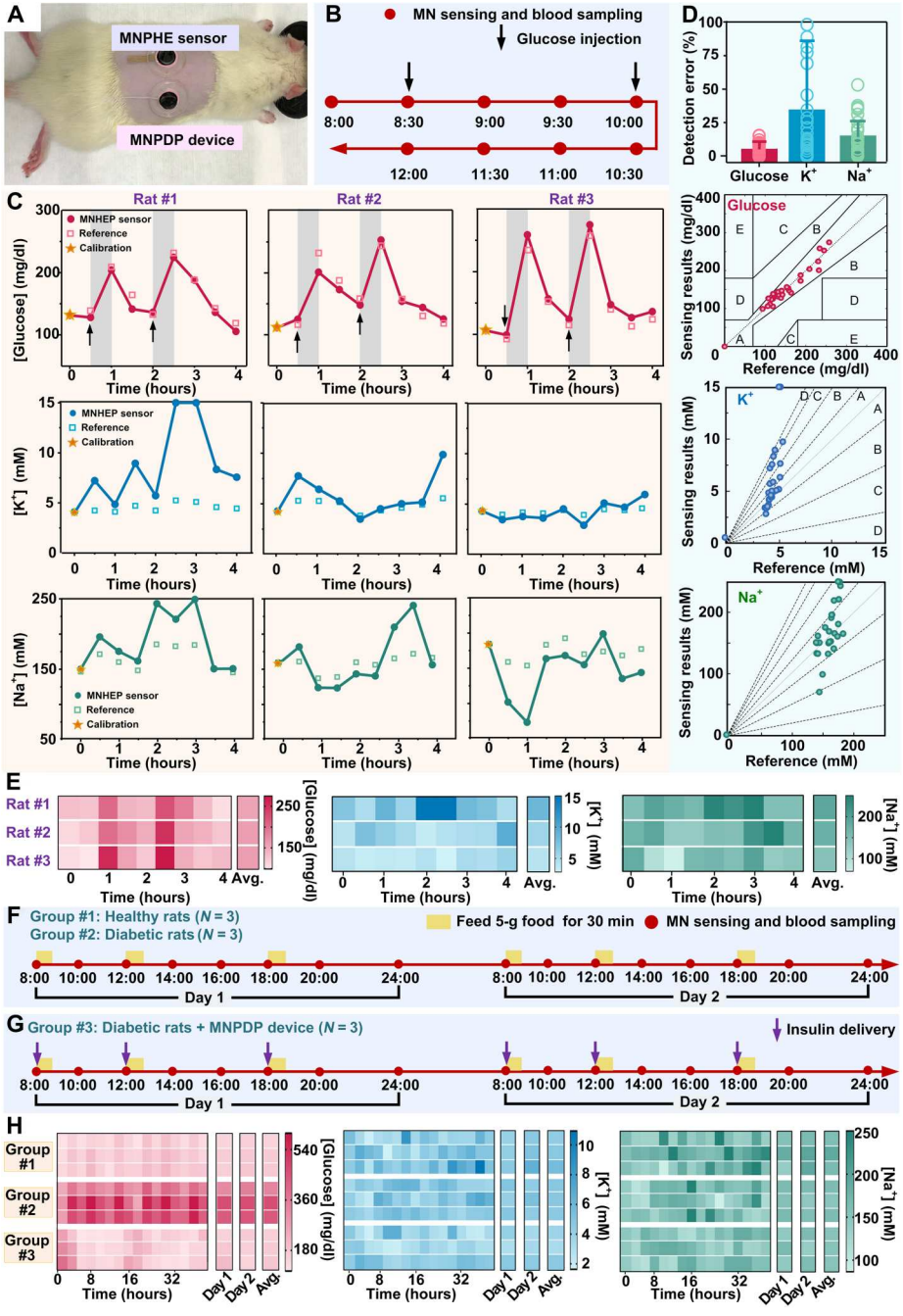

Fig. 5. Performance characterization of MNTP in vivo. (**A**) Photograph showing the simultaneous applications of the MNPHE sensor and MNPDP devices on a rat. (**B**) Timeline of the 4-hour detection experiment. (**C**) Dynamic glucose (top), K^+ (middle), and Na^+ (bottom) signals measured by MNPHE and standard reference methods on three individual rat samples. (**D**) Statistical analysis (top) showing the detection errors of MNPHE compared to the standard reference methods. $N = 3$ samples. Clarke's error grid analysis (the second panel) showing the detection accuracy of glucose by MNPHE, compared to the actual BGLs measured via a standard glucometer. Error grid analysis (the two bottom panels) showing the detection accuracy of K^+ and Na^+ by MNPHE, compared to the results measured via a biochemical analyzer. (**E**) Heatmap plots of dynamic fluctuation of glucose (left), K^+ (middle), and Na^+ (right) concentrations measured with MNPHE on three individual rats. (**F**) Timeline of the 48-hour detection experiment for group #1, group #2, and (**G**) group #3. (**H**) Heatmap plots of dynamic fluctuation of glucose (left), K^+ (middle), and Na^+ (right) concentrations measured via MNPHE on three experimental groups (each group used three rats in parallel).

vivo via MNPHE sensor were calibrated using the first-measured data point (at $t = 0$ min, indicated with yellow star). The fluctuation profiles of the detected glucose, K^+, and Na^+ concentrations were shown in Fig. 5C, respectively. Besides, all results were further presented with heatmap plots, scatter diagram, and radar map plots (Fig. 5E and figs. S29 to S31). On the basis of the results, the concentrations of the glucose, K^+, and Na^+ in ISF were successfully detected with the MNPHE sensor on all the three tested rats. The glucose concentration of the healthy rats was observed to increase rapidly in 30 min (indicated by the gray bands) right after glucose injection and then rapidly dropped to normal level within an hour due to their normal metabolism. The glucose fluctuations could also be visualized in the heatmap with color changes. The color blocks representing glucose injection were notably darker than other color blocks, indicating successful detection of elevated glucose. However, K^+ and Na^+ concentrations in ISF appeared to be unaffected by the glucose injection. It could be explained by that the transient glucose elevation was insufficient to affect the kidney and liver functions of healthy rats, which did not cause obvious perturbation of electrolyte levels in the body. The MNPHE sensors were observed to track the fluctuation of glucose and ion concentrations in a similar profile with the reference measurements. All data on the three rats were analyzed and compared to the reference measurements, where the accuracies were quantified and examined with error grid analysis. The errors of all the MNPHE sensor–measured glucose signals are below ~15.8%, with an average error of 5.92 ± 5.42% (Fig. 5D), which was close to the clinical requirements of glucose detection error. In addition, the average errors of K^+ and Na^+ are 32.7 ± 51.8% and 15.8 ± 13.2%, respectively (Fig. 5D). In the error grid analysis, all of the MNPHE sensor-measured data were located in region A, indicating excellent accuracy (figs. S32 and S33). These results demonstrated that the MNPHE sensor could successfully detect the concentration of glucose, K^+, and Na^+ from exudated ISF mediated by MN penetration with reasonable accuracy. However, without any calibration, the accuracy of MNPHE sensor was greatly reduced because of the vast difference between in vivo and in vitro environments (fig. S34).

In the second set of long-term experiment, the detections of three analytes (glucose, K^+, and Na^+) in ISF with MNPHE sensor were assessed on both healthy rats and streptozotocin-induced diabetic rats every 2 hours during daytime, totally lasting for 2 days (Fig. 5F). All rats were provided with three daily standardized meals at a comparatively fixed time (indicated with yellow bands). The rats were divided into three groups, where the group #1 of rats ($N = 3$) was in healthy state without insulin delivery during the whole experimental process. The group #2 of rats ($N = 3$) was suffering diabetes without insulin delivery, while the group #3 of rats was also in diabetic states but insulin delivery via MNPDP device was offered to regulate the hyperglycemia after each meal (Fig. 5G, indicated with purple arrows). Similar to the first experiment, the detection results in vivo via MNPHE sensors were calibrated every day (at $t = 0$ hours and $t = 24$ hours, indicated with yellow star). Reflected by the darker red, the glucose levels of the group #2 (diabetes without treatments) were higher than that in other two groups, and the postprandial glucose levels (the 2nd, 4th, 7th, 10th, 12th, and 15th points) were also notably higher than those on the other time points (Fig. 5H and fig. S35). The results indicated not only the impacts of diet composition amount on hyperglycemia but also the necessity of insulin intervention for persistently maintaining the normal glucose (*44*). The K^+ concentration of three groups was not observed discernible difference, while the Na^+ concentration of healthy rats is slightly higher than the other two groups involving diabetic rats. It might be explained that diabetes triggered a decline in kidney function, and the normal sodium retention function was impaired, followed by the decrease of blood sodium.

Overall, the fluctuation profiles of the detected glucose, K^+, and Na^+ concentrations for all the three tested groups were showed in Fig. 6 (A to C, respectively). The MNPHE sensors were observed to track the glucose and ion concentration in a similar profile with the reference measurements. In addition, all the data of analytes on the three groups were further analyzed and compared to the reference measurements, where the accuracies were quantified and assessed with error grid analysis (Fig. 6D). Almost all the detected results glucose located in region A, except for the glucose results in group #3, which had 87.5% data points in region A. The detection errors for glucose, K^+, and Na^+ concentrations in group #1 were 4.21 ± 2.73%, 23.70 ± 20.81%, and 15.93 ± 15.21%, respectively. The detection errors in group #2 were ~3.1% for glucose, ~19.8% for K^+, and ~15.8% for Na^+, while the detection errors in group #3 were ~5.7% for glucose, ~21.9% for K^+, and ~12.6% for Na^+, indicating that MNPHE sensors could detect the three analytes with satisfactory accuracy (Fig. 6E). The 48-hour average analyte concentrations and detection errors of three individual rats in each group were also plotted with radar map plots (fig. S36). While the same device was applied on a rat for repeating sensing eight times on each day, the repeated use of the sensor did not show obvious signal deviation after repeating usage (fig. S37). Although there was a lag time between the changes in ISF and plasma, it could be calibrated by algorithm in actual applications. These results indicated the MNPHE sensors could be applied for in situ glucose and electrolytes monitor on animals with satisfying reliable accuracy and performance. In addition, uses of more calibration points could further improve the sensing accuracy, compared with 0 calibration and once calibration (figs. S38 and S39).

To reveal the dynamic change process of various physiological indicators of diabetes complications, we comprehensively analyzed the postprandial changes of the glucose, K^+, and Na^+ (Fig. 6F and fig. S40). The results showed that the overall glucose concentrations of healthy rats fluctuated with food intake, where the glucose concentrations increased gradually within 2 hours after feeding but basically maintained within normal range. Same food supplement and monitoring modes were also performed on diabetic rats, which displayed intraday glucose fluctuations more obviously compared to the healthy rats. The postprandial changes of the glucose of group #2 (diabetic rats, Δglucose =146.45 ± 63.18 mg/dl) were greater than that of healthy rats (Δglucose =45.42 ± 16.77 mg/dl), which was likely associated with the insufficient insulin secretion of metabolic disorders. These results indicated that the diabetic rats with a traditional breakfast-lunch-dinner feeding pattern were in need of timely insulin supplement to avoid intermittent BGL increase. To control the glycemic fluctuations, we treated the diabetic rats in the group #3 with insulin delivery via MNPDP device immediately after each meal. These MNPDP-treated diabetic rats exhibited effective regulation of hyperglycemia after feeding (Δglucose = −11.85 ± 43.82 mg/dl), where the glucose concentrations maintained at the normoglycemic range during the whole experimental process. Nonetheless, the glucose concentrations in rats

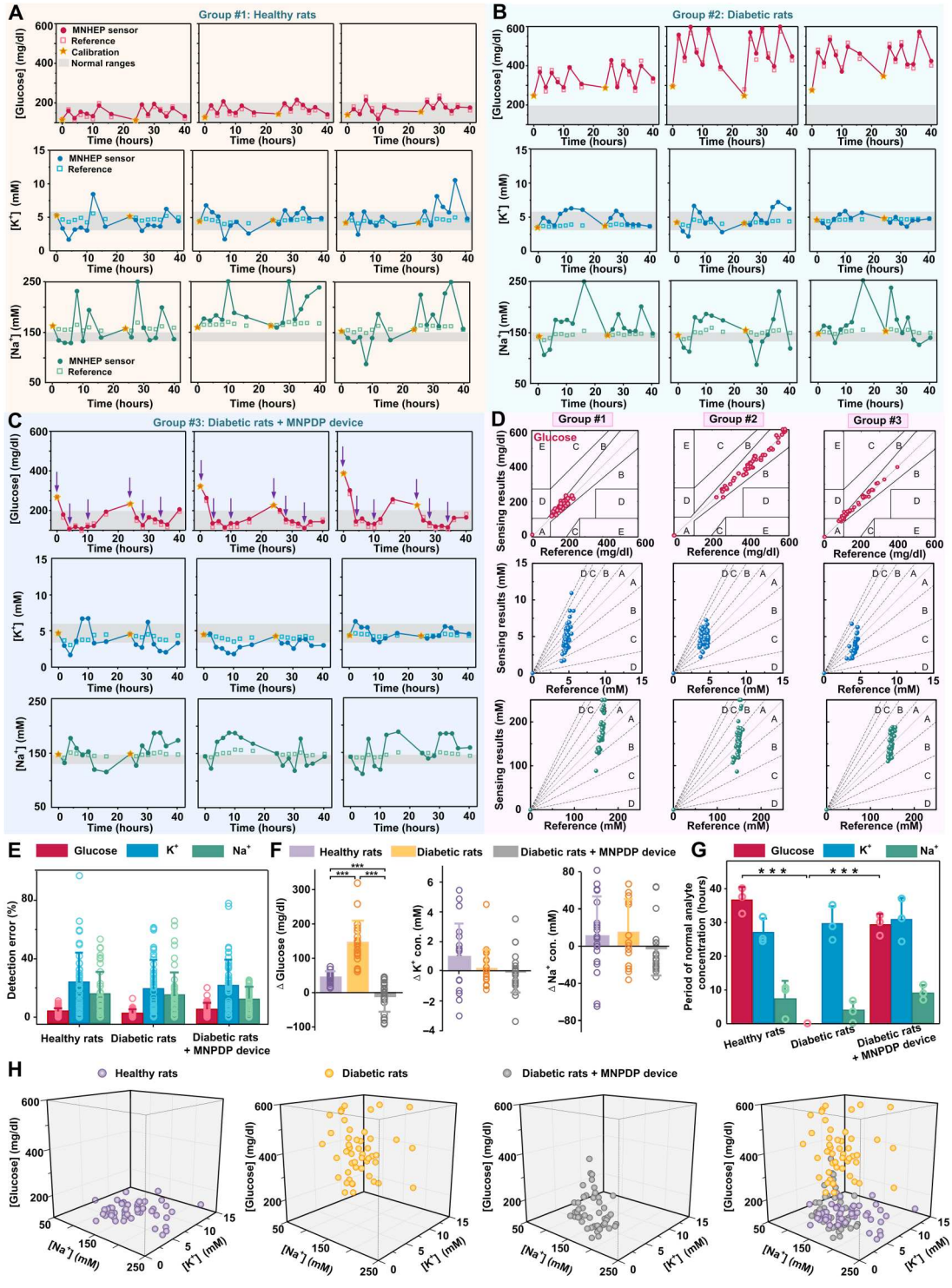

Fig. 6. Comprehensive analysis of MNTP in vivo for long-term application. (**A** to **C**) Dynamic fluctuation of glucose (top), K^+ (middle), and Na^+ (bottom) signals measured via MNPHE and reference methods on healthy rats (group #1), diabetic rats (group #2), and diabetic rats treated with MNPDP (group #3). (**D**) Clarke's error grid analysis (the top panel) showing the detection accuracy of glucose by MNPHE, compared to the actual BGLs measured via a standard glucometer. Error grid analysis (the two bottom panels) showing the detection accuracy of K^+ and Na^+ by MNPHE, compared to the actual results measured via a biochemical analyzer. (**E**) Statistical analysis showing the detection errors of MNPHE compared to the standard reference methods. $N = 3$ samples. (**F**) Statistical analysis of analyte concentration changes (Δglucose, ΔK^+, and ΔNa^+) within postprandial 2 hours. $N = 3$ samples. (**G**) Histogram of the period of normal analyte (glucose, K^+, and Na^+) concentrations; the three testing groups including healthy rats, diabetic rats, and diabetic rats treated with MNPDP. $N = 3$ samples. (**H**) 3D scatter diagram showing the correlation of in vivo glucose, K^+, and Na^+ concentrations for the three testing groups including healthy rats, diabetic rats, and diabetic rats treated with MNPDP. Each measuring point of each rat was presented.

tended to rebound to the hyperglycemia state after overnight insulin discontinuation, suggesting that the diabetic rats treated with MNPDP exhibited insulin-dependent hypoglycemic effect. Correspondingly, the serum insulin level of diabetic rats treated by MNPDP reached its maximum level at the 2nd hour after administration, ~17-fold higher than that of untreated diabetic rats (fig. S41). However, food intake only induced a small amount of variation of both K^+ and Na^+ concentrations. The K^+ concentration displayed a slight increase ($\Delta K^+ = 0.98 \pm 2.26$ mM) in the healthy rats group compared to group #2 by <5.2-fold and group #3 by <19.6-fold, while the delivery of insulin seemed to produce slight effects on the variation of K^+ concentration. On the other hand, the Na^+ concentration also displayed an increase ($\Delta Na^+ = 10.56 \pm 42.37$ mM) in the healthy rats group compared to the group #2 by <0.74-fold and group #3 by <2.1-fold, while the delivered insulin induced little variation of Na^+ concentration. Reduction of postprandial ions was likely due to the fact that the diabetic symptoms of polyphagia, polydipsia, polyuria, and emaciation resulted in more K^+ and Na^+ consumption and less K^+ and Na^+ retention.

Furthermore, we defined normal range of three analytes to dig out more details of diabetes for clinical treatment. For example, 100 to 200 mg/dl, 3.2 to 5.7 mM, and 133 to 146 mM were set as the normal ranges of glucose, K^+, and Na^+, which is the most widely accepted in many literatures (*25*, *45*, *46*). The time in normal states of glucose, K^+, and Na^+ in untreated diabetic rats is 0, 30.30 ± 5.35, 3.93 ± 2.68 hours, respectively (Fig. 6G). The normal time in MNPDP-treated diabetic rats, by contrast, all have been notably improved, with the 29.33 ± 3.1 hours of glucose, 30.67 ± 6.51 hours for K^+, and 9.2 ± 2.31 hours for Na^+. These results demonstrated that the in-time and on-demand insulin treatments via MNPDP device could inhibit postprandial glycemic increases due to meal consumption, which was effective in the therapy of diabetes. To further understand the correlation between the three analytes, the distributions of all measuring points were mapped with 3D plots (Fig. 6H). For the healthy rats, the detection points were concentrated in the bottom, while the detection points for the diabetes group were distributed in the top, corresponding to the higher glucose. However, the detection points in the MNPDP-treated diabetes group were closer to the area of the healthy rats group, indicating the normalization of three indicators. Besides, the in vivo biosafety of MNs of the MNTP were evaluated by the recovery and histological examination of the MN-inserted skins (figs. S42 to S44). The micropores punctured by MNs could disappeared within 18 min for a single insertion and 32 min for five insertions. The back skin of rats was also repeated punctured by MN once an hour and total 10 times per day for several consecutive days (0, 1, 3, and 5 days). On the basis of the histological studies, no obvious density increases in the infiltrating inflammatory cells in the skins treated by MN compared to untreated skin, even after the repeated MN penetration.

DISCUSSION

In this work, a biomimetic nonimplanting MNTP for simultaneous sensing and insulin delivery in a closed-loop manner was developed for the treatment of diabetes. This system was inspired by the feature of animal masticatory system, which consisted of masseter muscle, teeth, tongue, and oral mucosa that could fulfill the functions of tissue penetration, taste sensing, and saliva secretion. Similar to the animal masticatory system, the biomimetic MNTP used MN arrays for controllable penetration of skin layer in a pain-free manner, which enabled ISF exudation to the MN-integrated epidermal sensor arrays for simultaneous detection of glucose and ions. The sensing results could be feedbacked to trigger insulin delivery following MN penetration. The MN-based sensor and the drug delivery device were integrated with miniatured circuits as a closed-loop system, which could automatically control the mechanical pressing of MNs and drug delivery through an integrated peristaltic pump. The nonimplanting features of the MNs could effectively avoid the biosafety and stability issue of electrodes for long-term implantation. The ISF exudation feature could address the challenge of limited electrode surface area and "oxygen-deficit" issues in vivo, while the integrated epidermal sensor patch could be flexibly functionalized with hybrid carbon nanomaterials as electron mediator to improve sensitivity. The MNTP was demonstrated to accurately detect both glucose and ions and deliver insulin to regulate hyperglycemia, which enabled long-term monitoring and on-demand therapy. The biomimetic, smart, and closed-loop features of the MNTP endowed this system as a highly advanced system for facilitating diabetes treatments and could be potentially extended for the therapies on a variety of chronic diseases.

MNTP consisting of an MNPHE sensor and an MNPDP device could simultaneously track multiple biomarkers in situ and provide controlled drug delivery to treat hyperglycemia and its complications, which were crucial for an intelligent system of diabetic theranostic. Besides, MNPHE sensor could monitor the analytes with reliable accuracy, while MNPDP device could accordingly adjust the drug release dose in real time based on the direct feedback–detected data via a self-built control algorithm. Thereby, the analyte and drug levels could fluctuate within the expected safe therapeutic range. In brief, such MN-mediated MNTP could realize the exact detection of multiphysiological signals, optimal calculation of drug doses, and intelligent delivery of drugs in a closed-loop controllable manner.

MATERIALS AND METHODS

Materials

CNT/isopropanol slurry (TNAPM-M8) was purchased from Chengdu Organic Chemicals Co. Ltd. GO aqueous solution (Carmery) was purchased from the Institute of Coal Chemistry, Chinese Academy of Science. Ag/AgCl conductive inks were purchased from ALS Co. Ltd. All of the following chemicals were obtained from Sigma-Aldrich: BSA, glutaraldehyde solution, selectophore grade sodium ionophore X, sodium tetrakis [3,5-bis(-trifluoromethyl)phenyl] borate (Na-TFPB), valinomycin (potassium ionophore), sodium tetraphenylborate (NaTPB), bis(2-ethylehexyl) sebacate (DOS), high–molecular weight polyvinyl chloride (PVC), tetrahydrofuran, cyclohexanone, dimethyl sulfoxide, polyaniline emeraldine, sodium chloride (NaCl), and Gox (from *Aspergillus niger*). All the chemicals were used as received. All solutions were prepared using deionized water (18.3 megohm·cm) produced from a Millipore water purification system, unless otherwise noted. The peristaltic pump was purchased from Aquatech Co. Ltd. (Osaka, Japan), which mainly consists of a motor, a pump head, and a tube. The tube is fixed between the pump head and the pump case. The motor drives the pump head to rotate, which alternately squeezes and releases the tube to pump

fluid. As the pump head rotates, negative pressure forms inside the tube, which allows the liquid to flow through the tube.

Fabrication of Pt NPs/CNT-rGO/Au hybrid electrodes

The PET (200 μm) was punched by ultraviolet laser (UV-3S, Han′s Laser Technology Industry Group Co. Ltd), aligning as array corresponding to the MN layout. The sensor arrays on PET were covered with a patterned mask, followed by 30 nm of Cr/50 nm Au deposition by the magnetron sputtering machine (MSP-3300, Jinshengweina Technology Co. Ltd., China). Nanostructural CNT-rGO was prepared on the sensor surface via a layer-by-layer assembly method followed by chemical reduction. The CNT/isopropanol slurry with 8.6 weight percent (wt %) CNTs and aqueous solution containing GO (6 mg/ml) were uniformly mixed at a volume ratio of 1:1. The mixed CNT-GO solution was conformally coated on the surface of patterned Au layer and dried. The nonconductive GO on the surface was then reduced to be conductive rGO by immerging the electrode into aqueous solution of vitamin C solution (10 mg/ml) at 95°C for 3 hours. Then, CNT-rGO electrode arrays were washed with deionized water three times to remove impurities. After we dried it in room temperature, Pt NPs electrodeposited on the electrode using multicurrent steps at the current of −1 mA for 200 s in the mixed solution (8 mM H_2PtCl_6 and 50 mM HCl). Last, three independent W.E were fabricated on the same substrate, which were further functionalized with respective enzymes or ion-selective membranes for the detection of glucose, Na^+, and K^+. The Ag/AgCl R.Es were obtained by coating Ag/AgCl conductive inks and encapsulated with PVB.

Preparation of K^+ and Na^+ hybrid electrodes

Typically, the cocktail of Na^+-selective membrane was prepared consisting of Na ionophore X (1% weight by weight, w/w), Na-TFPB (0.55%, w/w), PVC (33%, w/w), and DOS (65.45%, w/w). The cocktail (200 mg) was dissolved in 1320 μl of tetrahydrofuran with shaking on a shaker for 30 min. For the K^+-selective membrane, the cocktail was composed of valinomycin (2%, w/w), NaTPB (0.5%), PVC (32.7%, w/w), and DOS (64.7%, w/w). The cocktail (200 mg) was dissolved in 700 μl of cyclohexanone to obtain membrane solution. All the ion-selective solutions were sealed and stored at 4°C when not used. Ion-selective membranes were then prepared by drop-casting 5 μl of the Na^+- and K^+-selective membrane cocktail onto their corresponding electrodes. Then, the electrodes were allowed to dry overnight in ambient environment.

Preparation of hybrid glucose electrodes

GOx solution (50 mg/ml), BSA solution (80 mg/ml), and glutaraldehyde solution (2.5%) were mixed at the volume ratio of 1:5:2. Then, 5 μl of the mixed solution was coated onto the electrode and dried overnight, followed by being rinsed with deionized water to remove the redundant solution.

Assembly of MNPHE sensor

The MN array was fabricated by mature micromilling technology. The computer software was used to draft the shape and structure of MN arrays. Subsequently, the MNs were cut using the precision machine tool with high rotation speed, followed by electropolishing and cleaning. A PDMS-made button, medical tape, a gasket, an MN array, a medical sponge, a Pt NPs/CNT-rGO/Au hybrid electrode, and a buffering layer are concentrically bonded together using a thin layer of light-curing resin (white resin, Formlabs). The holes array of hybrid electrode was aligned with the MN array so that MNs can be exactly penetrated through the holes.

Assembly of MNPDP device

Similar with the MNPHE sensor, the PDMS-made button, medical tape, a gasket, an MN array, and a medical sponge were glued together using a thin layer of light-curing resin. A channel (outer diameter ~ 1 mm) was drilled in the side of the gasket for the placement of a drug tube, which was made of flexible silicon. The drug tube is tightly connected to the peristaltic micropump tube with a suitable connector. The electronics, micropump, and drug reservoir were housed in a polypropylene box (9 cm by 6 cm by 3 cm).

Design of PCB

The Na^+ and K^+ hybrid electrodes can reflect ion concentration by outputting different open circuit voltages. To realize this function, the differential amplification modules with high input impedance and low output impedance was used for signal amplification and common-mode interference reduction. The glucose electrodes detect glucose concentration in ISF via amperometric method. A precision op-amp, with low input bias current, low offset voltage, and low offset voltage temperature drift, was applied as voltage follower and transimpedance amplifier to meet the requirements of constant potential circuit. By maintaining the reverse potential of C.E, the voltage between R.E and W.E was kept stable to improve the accuracy of corresponding current detected by the glucose sensor. STM32F103C8T6 microcontroller (ARM 32-bit) was used to the core of the MCU, which could be programmed on-board through Serial Wire Debug interface. In this unit, the analog digital converter was used to detect the amplified signals of the MNPHE sensor, while the DAC provided a suitable reference voltage for the constant potential module. The flow rate of peristaltic micropumps and the switch of the pressuring components could be controlled through the control Input/Output (I/O). In addition, communication with the computer and Bluetooth module (low-power Bluetooth chip CC2640R2F) could be realized in serial ports. A motor drive chip was applied to control the flow rate of pumps by providing appropriate frequency and different duty cycle PWM waveform. As for the pressing belt, it was controlled by a relay switch via I/O. A 5-V power supply was provided by the Universal Serial Bus for the circuit. Then, the voltage was regulated to +3.3 V for microcontroller and Bluetooth module and ± 5 V for op-amp chips and the motor driver chip.

In vitro electrochemical performance of MNPHE sensors

All electrochemical experiments were conducted on the CHI660E electrochemical workstation (Shanghai Chenghua Instrument Co. Ltd., Shanghai, China). The sensitivity, selectivity, reproducibility, and stability of each electrode were evaluated. For the glucose hybrid electrode: (i) The sensitivity: The electrode was immersed in a phosphate-buffered saline (PBS) solution, where the glucose concentration was increased by stepwise of 2 up to 22 mM. A bias voltage of 0.5 V was applied to the electrode, and the current signal was recorded. (ii) The selectivity was tested by successive addition of interferents in PBS solution. (iii) The reproducibility was investigated by recording the currents of five glucose electrodes in same glucose solution of 0, 4, 8, 12, and 16 mM. (iv) The long-term stability: Three glucose electrodes were stored at 4°C, and their

amperometric response was measured in 10 mM glucose solution every 2 days. For the K^+ hybrid electrode: (i) The sensitivity: The K^+ electrode was immersed in the 1 mM KCl solutions, where the concentration was increased twice each time until 32 mM, and the potentiometric signal was recorded. (ii) The selectivity was evaluated by sequential addition of multiple interfering electrolytes to 2 mM KCl solution. (iii) The reproducibility was investigated by recording the potentials of 5 K^+ electrodes in the KCl solution of 1, 2, 4, 8, 16, and 32 mM. (iv) The long-term stability: Three K^+ hybrid electrodes were stored at 4°C and measured their sensitivities every 2 days. For the Na^+ hybrid electrode: i) The sensitivity: The Na^+ electrode was immersed in the 5 mM NaCl solutions, where the concentration was increased twice each time until 160 Mm, and the potentiometric signal was recorded. (ii) The selectivity was evaluated by sequential addition of multiple interfering electrolytes to 10 mM NaCl solution. (iii) The reproducibility was investigated by recording the potentials of five Na^+ electrodes in the NaCl solution of 5, 10, 20, 40, 80, and 160 mM. (iv) The long-term stability was evaluated according to the method of K^+ hybrid electrodes. The CV curves were obtained using CV method with scan rate of 100 mV/s and 12 sweep segments.

Mechanical penetration tests of MNs

A customized test equipment was designed for mechanical tests, as illustrated in the Supplementary Materials. The skin penetration process was performed by mimicking the "press and release" action on porcine skin. The MNPDP device was gradually pressed at 4 mm, held for 10 s, and subsequently released the compression. Both press and release velocities are 0.1 mm/s. The MNPDP device was filled with rhodamine B (0.4 wt %, 200 μl) solution in the porous reservoir. After the MNPDP device was pressed against porcine skin and then withdrawn for 10 min, the porcine skin was observed.

Compression performance of the pressing belt

The MNPDP device was wrapped on a silica gel hand model by pressing belt, and a piece of porcine skin was padded between them. A resistive thin-film pressure sensor was placed between the belt and the hand model and connected with multichannel source meter (Keithley 2636B) to record the force-time curve. Each cycle contained 40 s of inflation and 20 s of deflation and was repeated more than five times. Then, the punctured porcine skin was stained with rhodamine B (0.4 wt %) solution, and then the excess dye on the surface was washed off. Last, the skin was observed using a fluorescence microscope (MF53-N) at 540-nm excitation light.

In vitro transdermal drug delivery

The permeation studies of calcein and insulin through the porcine skin were performed using vertical Franz diffusion cells (TP-3A, Albert Tech., China). The receptor chambers was fully filled with PBS and stirred constantly at 37°C. The upper donor chambers was filled with calcein (20 μg/ml, 2 ml) and insulin (1 mg/ml, 2 ml), respectively. The receptor fluid was continuously, magnetically stirred at 280 rpm. Samples were withdrawn through the sampling port at predetermined time intervals, and the receptor chamber phase was immediately replenished with an equal volume of fresh PBS buffer to maintain a constant volume. The concentration of insulin was measured by Coomassie blue method, and the absorbance at 595 nm was detected on a microplate reader (M200PRO, infinite). The insulin concentration was calibrated by a standard curve. The concentration of calcein was measured by the microplate reader at the excitation wavelength of 485 nm and the emission wavelength of 535 nm.

Theoretical calculation via COMSOL Multiphysics 5.5 simulation

The models were constructed by COMSOL Multiphysics 5.5 using the Creeping flow module and Chemical Species Transport module. The liquid insulin is continuously transported through the bottom of skin to the systemic circulation. The drug diffusion concentration at the bottom of skin was set as 0. After releasing, the average insulin concentration in the interstitial space was calculated to evaluate the delivery efficiency. The related physical parameters for simulation include the following: (i) the insulin diffusion coefficients in the SC, epidermis, dermis, and sponge; (ii) initial concentrations of insulin in the sponge; (iii) the density and kinetic viscosity of skin, sponge, MN array, and microholes; and (iv) the normal inflow velocity of insulin through the drug tube. The detailed physic setting of insulin delivery, related parameters, and the governing equations can be found in the Supplementary Materials. A Transport of Diluted Species module was used to compute the transient concentration distribution, following the controlling equations

$$\frac{\partial c_i}{\partial t} + \nabla \bullet \boldsymbol{J}_i + \boldsymbol{u} \bullet \nabla c_i = R_i \tag{1}$$

$$\boldsymbol{J}_i = -D_i \nabla c_i \tag{2}$$

where c_i refers to concentration, $\boldsymbol{J}_i$ is the flux, $\boldsymbol{u}$ is the flow velocity, R_i refers to reaction rate, D_i is the diffusion coefficient, and ∇ refers to the Hamiltonian operator. Next, time-dependent study was used to simulate the dynamic pumping process via Creeping Flow module, ignoring the inertia term. The govern equation was as below

$$\rho \frac{\partial \boldsymbol{u}}{\partial t} + \rho(\boldsymbol{u} \bullet \nabla)\boldsymbol{u} = \nabla \bullet [-p\boldsymbol{I} + \boldsymbol{K}] + F \tag{3}$$

$$\rho \nabla \bullet \boldsymbol{u} = 0 \tag{4}$$

where ρ refers to density, $\boldsymbol{u}$ is the velocity vector, p is the pressure, **F** refers to volume force vector, D_i is the diffusion coefficient, and **K** is the Lagrange multipliers that are used to implement the boundary condition.

Experimental animals

All animal procedures conducted in this work were reviewed, approved, and supervised by the Institutional Animal Care and Use Committee (IACUC) at the Sun Yat-Sen University (approval number: SYSU-IACUC-2021-000022, SYSU-IACUC-2021-000020, and SYSU-IACUC-2021-000612). Male Sprague-Dawley rats weighing 200 to 250 g were purchased from Animal Center of Sun Yat-sen University, Guangzhou, China) were used for experiments. Rats were housed in a climate-controlled room under a 12-hour light/12-hour dark cycle and with food and water. Streptozotocin (Sigma-Aldrich) at a dose of 60 mg/kg was used to induce type 1 diabetes rats. Their BGLs were detected for at least 7 days. The rats with a BGL that was kept steady over 300 mg/dl were induced successfully.

Application of MNPHE sensors and MNPDP devices on rats

The rats were anesthetized with 2% isoflurane gas using an anesthesia system (C90, RIDTER, Beijing, China) via a nose cone, and the hairs on the back were removed by hair removal cream (VEET depilatory cream, Reckitt Benckiser). The MNPHE sensors and MNPDP devices were fixed on the back of rats by bandages, remaining stable during the whole test process. For short-term monitoring of healthy rats, glucose fluctuations were induced at different time points (at 30 and 120 min) by an intraperitoneal injection of 3 ml of glucose solution (5%). Glucose levels and K^+ and Na^+ concentrations were detected via MNPHE sensors every 30 min. At each measurement, MN was manually pressed on the rats′ skin for 1 min to penetrate the SC. The MNs were withdrawn into the sponge, while the MNPHE was pressed onto the skin to detect the glucose, K^+, and Na^+ concentrations. Blood was drawn from the tail tip of the rat at same time points (0, 30, 60, and 90 min) to measure the BGLs by a standard Roche BGL meter (Accu-Chek Performa) and to measure K^+ and Na^+ concentrations by a small animal biochemical analyzer (iMagic-V7, ICUBIO). The glucose, K^+, and Na^+ levels detected via MNPHE sensors were compared to the actual for quantifying the detection accuracies and were examined with error grid analysis. For long-term monitoring (48 hours) of healthy and diabetic rats, they were provided three daily standardized meals at a comparatively fixed time (breakfast at 08:00, lunch at 12:00, and dinner at 18:00). Each meal took 30 min for eating, and the remaining food will be removed. The insulin delivery was implemented by MNPDP devices. The glucose, K^+, and Na^+ concentrations were measured by MNPHE at set time points (at 08:00, 10:00, 12:00, 14:00, 16:00, 18:00, 20:00, and 24:00). At the meantime, blood was drawn from the tail tip of the rat at same time points to measure the BGLs and reference K^+ and Na^+ concentrations by commercial instruments. For the ion calibration method in vivo, the voltage signals (V_{nm}, n = 0, 1, 2, 3, 4....) measured by MNTP was converted to the ion concentration (C_{nm}, n = 0, 1, 2, 3, 4....) by the in vitro standard curve $V_{nm} = A + B * \lg(C_{nm})$. The ion concentration in the tail venous blood measured by standard reference methods was expressed as C_{nr}. The ratio of initial C_{0r} and initial blood ion concentration C_{0m} was used as calibration coefficient β, namely, $\beta = C_{0m}/C_{0r}$. Then, all C_{nm} was calibrated by multiplying β as final concentration results. Considering the actual concentration ranges of K^+ and Na^+ in vivo, the upper and bottom concentration range of Na^+ in vivo detected by MNTP was set to be 50 and 250 mM, while the upper and bottom concentration range of K^+ in vivo detected by MNTP was set to be 0 and 15 mM. For measured K^+ and Na^+ concentration signals exceeding this range, the final calculated concentrations were converted to either the upper concentration value or the bottom concentration value. For insulin delivery, the insulin solution (50 IU/ml) was loaded in the drug reservoir connected with the micropump. Immediately after eating, diabetic rats were treated with insulin. The voltage of the micropumps was set to 3 V for 1 min for insulin infusion into the sponge, which would further diffuse into the subcutaneous space through diffusion for 1 hour.

Morphology characterization methods

The MN array was characterized using a scanning electron microscope (Phenom Pro Desktop SEM, Thermal Fisher Scientific) and a super depth of field microscope (VHX-7000, KEYENCE). The punctured skin by MN array was observed by SEM, OCT (HSO-2000, TEK SQRAY, China), and microscope (BX51 M, Olympus, Japan). The W.E of Pt NPs/CNT-rGO/Au hybrid electrodes was observed using an SEM (SUPRA 60, Zeiss). The surface element analysis of Pt NPs/CNT-rGO/Au hybrid electrodes was performed using EDX (Oxford Instrument).

Statistical analysis

The data were calculated and expressed as the means ± SD. The differences between the two compared groups were determined by Student′s t test. P values of <0.05 indicated that the results were considered statistically significant. $^*P < 0.05$, $^{**}P < 0.01$, and $^{***}P < 0.001$.

Supplementary Materials

This PDF file includes:

Supplementary Text
Figs. S1 to S44
Tables S1 and S2
References

View/request a protocol for this paper from *Bio-protocol*.

REFERENCES AND NOTES

1. J. Yu, J. Wang, Y. Zhang, G. Chen, W. Mao, Y. Ye, A. R. Kahkoska, J. B. Buse, R. Langer, Z. Gu, Glucose-responsive insulin patch for the regulation of blood glucose in mice and minipigs. *Nat. Biomed. Eng.* **4**, 499–506 (2020).
2. W. Chen, R. Tian, C. Xu, B. C. Yung, G. Wang, Y. Liu, Q. Ni, F. Zhang, Z. Zhou, J. Wang, G. Niu, Y. Ma, L. Fu, X. Chen, Microneedle-array patches loaded with dual mineralized protein/peptide particles for type 2 diabetes therapy. *Nat. Commun.* **8**, 1777 (2017).
3. Y. Zhang, J. Yu, A. R. Kahkoska, J. Wang, J. B. Buse, Z. Gu, Advances in transdermal insulin delivery. *Adv. Drug Deliv. Rev.* **139**, 51–70 (2019).
4. W.-L. Hsu, C.-Y. Huang, Y.-P. Hsu, T.-L. Hwang, S.-H. Chang, H.-Y. J. Wang, L.-Y. Feng, S.-J. Tzoug, K.-C. Wei, H.-W. Yang, On-skin glucose-biosensing and on-demand insulin-zinc hexamers delivery using microneedles for syringe-free diabetes management. *Chem. Eng. J.* **398**, 125536 (2020).
5. X. Li, X. Huang, J. Mo, H. Wang, Q. Huang, C. Yang, T. Zhang, H.-J. Chen, T. Hang, F. Liu, L. Jiang, Q. Wu, H. Li, N. Hu, X. Xie, A fully integrated closed-loop system based on mesoporous microneedles-iontophoresis for diabetes treatment. *Adv. Sci. (Weinh)* **8**, e2100827 (2021).
6. X. Xie, J. C. Doloff, V. Yesilyurt, A. Sadraei, J. J. McGarrigle, M. Omami, O. Veiseh, S. Farah, D. Isa, S. Ghani, I. Joshi, A. Vegas, J. Li, W. Wang, A. Bader, H. H. Tam, J. Tao, H.-J. Chen, B. Yang, K. A. Williamson, J. Oberholzer, R. Langer, D. G. Anderson, Reduction of measurement noise in a continuous glucose monitor by coating the sensor with a zwitterionic polymer. *Nat. Biomed. Eng.* **2**, 894–906 (2018).
7. S. R. Yurista, C.-R. Chong, J. J. Badimon, D. P. Kelly, R. A. de Boer, B. D. Westenbrink, Therapeutic potential of ketone bodies for patients with cardiovascular disease: JACC state-of-the-art review. *J. Am. Coll. Cardiol.* **77**, 1660–1669 (2021).
8. S. Arora, D. Cheng, B. Wyler, M. Menchine, Prevalence of hypokalemia in ED patients with diabetic ketoacidosis. *Am. J. Emerg. Med.* **30**, 481–484 (2012).
9. P. R. Miller, X. Xiao, I. Brener, D. Bruce Burckel, R. Narayan, R. Polsky, Microneedle-based transdermal sensor for on-chip potentiometric determination of K^+. *Adv. Healthc. Mater.* **3**, 876–881 (2014).
10. Y. Zheng, R. Omar, R. Zhang, N. Tang, M. Khatib, Q. Xu, Y. Milyutin, W. Saliba, Y. Y. Broza, W. Wu, M. Yuan, H. Haick, A wearable microneedle-based extended gate transistor for real-time detection of sodium in interstitial fluids. *Adv. Mater.* **34**, e2108607 (2022).
11. T. M. Blicharz, P. Gong, B. M. Bunner, L. L. Chu, K. M. Leonard, J. A. Wakefield, R. E. Williams, M. Dadgar, C. A. Tagliabue, R. E. Khaja, S. L. Marlin, R. Haghgooie, S. P. Davis, D. E. Chickering, H. Bernstein, Microneedle-based device for the one-step painless collection of capillary blood samples. *Nat. Biomed. Eng.* **2**, 151–157 (2018).
12. J. Kim, M. Kim, M.-S. Lee, K. Kim, S. Ji, Y.-T. Kim, J. Park, K. Na, K.-H. Bae, H. K. Kim, F. Bien, C. Y. Lee, J.-U. Park, Wearable smart sensor systems integrated on soft contact lenses for wireless ocular diagnostics. *Nat. Commun.* **8**, 14997 (2017).
13. M. Bariya, H. Y. Y. Nyein, A. Javey, Wearable sweat sensors. *Nat. Electron* **1**, 160–171 (2018).
14. W. Gao, S. Emaminejad, H. Y. Y. Nyein, S. Challa, K. Chen, A. Peck, H. M. Fahad, H. Ota, H. Shiraki, D. Kiriya, D.-H. Lien, G. A. Brooks, R. W. Davis, A. Javey, Fully integrated wearable sensor arrays for multiplexed in situ perspiration analysis. *Nature* **529**, 509–514 (2016).

15. R. M. Torrente-Rodríguez, J. Tu, Y. Yang, J. Min, M. Wang, Y. Song, Y. Yu, C. Xu, C. Ye, W. W. IsHak, W. Gao, Investigation of cortisol dynamics in human sweat using a graphene-based wireless mHealth system. *Matter* **2**, 921–937 (2020).
16. M. S. Mannoor, H. Tao, J. D. Clayton, A. Sengupta, D. L. Kaplan, R. R. Naik, N. Verma, F. G. Omenetto, M. C. McAlpine, Graphene-based wireless bacteria detection on tooth enamel. *Nat. Commun.* **3**, 763 (2012).
17. J. Kim, G. Valdés-Ramírez, A. J. Bandodkar, W. Jia, A. G. Martinez, J. Ramírez, P. Mercier, J. Wang, Non-invasive mouthguard biosensor for continuous salivary monitoring of metabolites. *Analyst* **139**, 1632–1636 (2014).
18. O. Veiseh, B. C. Tang, K. A. Whitehead, D. G. Anderson, R. Langer, Managing diabetes with nanomedicine: Challenges and opportunities. *Nat. Rev. Drug Discov.* **14**, 45–57 (2015).
19. R. Nimri, T. Battelino, L. M. Laffel, R. H. Slover, D. Schatz, S. A. Weinzimer, K. Dovc, T. Danne, M. Phillip, Insulin dose optimization using an automated artificial intelligence-based decision support system in youths with type 1 diabetes. *Nat. Med.* **26**, 1380–1384 (2020).
20. S. Kusama, K. Sato, Y. Matsui, N. Kimura, H. Abe, S. Yoshida, M. Nishizawa, Transdermal electroosmotic flow generated by a porous microneedle array patch. *Nat. Commun.* **12**, 658 (2021).
21. J. Yang, H. Zhang, T. Hu, C. Xu, L. Jiang, Y. S. Zhang, M. Xie, Recent advances of microneedles used towards stimuli-responsive drug delivery, disease theranostics, and bioinspired applications. *Chem. Eng. J.* **426**, 130561 (2021).
22. Q. Jin, H.-J. Chen, X. Li, X. Huang, Q. Wu, G. He, T. Hang, C. Yang, Z. Jiang, E. Li, A. Zhang, Z. Lin, F. Liu, X. Xie, Reduced graphene oxide nanohybrid-assembled microneedles as minimally invasive electrodes for real-time transdermal biosensing. *Small* **15**, e1804298 (2019).
23. M. R. Prausnitz, R. Langer, Transdermal drug delivery. *Nat. Biotechnol.* **26**, 1261–1268 (2008).
24. M. Dervisevic, M. Alba, L. Yan, M. Senel, T. R. Gengenbach, B. Prieto-Simon, N. H. Voelcker, Transdermal electrochemical monitoring of glucose via high-density silicon microneedle array patch. *Adv. Funct. Mater.* **32**, 2009850 (2021).
25. J. Yang, Y. Li, R. Ye, Y. Zheng, X. Li, Y. Chen, X. Xie, L. Jiang, Smartphone-powered iontophoresis-microneedle array patch for controlled transdermal delivery. *Microsyst. Nanoeng.* **6**, 112 (2020).
26. P. Makvandi, R. Jamaledin, G. Chen, Z. Baghbantaraghdari, E. N. Zare, C. Di Natale, V. Onesto, R. Vecchione, J. Lee, F. R. Tay, P. Netti, V. Mattoli, A. Jaklenec, Z. Gu, R. Langer, Stimuli-responsive transdermal microneedle patches. *Mater. Today* **47**, 206–222 (2021).
27. J. Wang, Z. Wang, J. Yu, A. R. Kahkoska, J. B. Buse, Z. Gu, Glucose-responsive insulin and delivery systems: Innovation and translation. *Adv. Mater.* **32**, e1902004 (2020).
28. H. Teymourian, F. Tehrani, K. Mahato, J. Wang, Lab under the skin: Microneedle based wearable devices. *Adv. Healthc. Mater.* **10**, e2002255 (2021).
29. H. Teymourian, M. Parrilla, J. R. Sempionatto, N. F. Montiel, A. Barfidokht, R. Van Echelpoel, K. De Wael, J. Wang, Wearable electrochemical sensors for the monitoring and screening of drugs. *ACS Sens.* **5**, 2679–2700 (2020).
30. H. Lee, T. K. Choi, Y. B. Lee, H. R. Cho, R. Ghaffari, L. Wang, H. J. Choi, T. D. Chung, N. Lu, T. Hyeon, S. H. Choi, D.-H. Kim, A graphene-based electrochemical device with thermoresponsive microneedles for diabetes monitoring and therapy. *Nat. Nanotechnol.* **11**, 566–572 (2016).
31. J. Gao, W. Huang, Z. Chen, C. Yi, L. Jiang, Simultaneous detection of glucose, uric acid and cholesterol using flexible microneedle electrode array-based biosensor and multi-channel portable electrochemical analyzer. *Sensor Actuat. B Chem.* **287**, 102–110 (2019).
32. X. Feng, H. Cheng, Y. Pan, H. Zheng, Development of glucose biosensors based on nanostructured graphene-conducting polyaniline composite. *Biosens. Bioelectron.* **70**, 411–417 (2015).
33. Y. Lin, M. Bariya, H. Y. Y. Nyein, L. Kivimäki, S. Uusitalo, E. Jansson, W. Ji, Z. Yuan, T. Happonen, C. Liedert, J. Hiltunen, Z. Fan, A. Javey, Porous enzymatic membrane for nanotextured glucose sweat sensors with high stability toward reliable noninvasive health monitoring. *Adv. Funct. Mater.* **29**, e1902521 (2019).
34. J. Lai, Y. Yi, P. Zhu, J. Shen, K. Wu, L. Zhang, J. Liu, Polyaniline-based glucose biosensor: A review. *J. Electroanal. Chem.* **782**, 138–153 (2016).
35. S. Vaddiraju, A. Legassey, Y. Wang, L. Qiang, D. J. Burgess, F. Jain, F. Papadimitrakopoulos, Design and fabrication of a high-performance electrochemical glucose sensor. *J. Diabetes Sci. Technol.* **5**, 1044–1051 (2011).
36. J. S. Del Rio, O. Y. F. Henry, P. Jolly, D. E. Ingber, An antifouling coating that enables affinity-based electrochemical biosensing in complex biological fluids. *Nat. Nanotechnol.* **14**, 1143–1149 (2019).
37. H. Teymourian, A. Barfidokht, J. Wang, Electrochemical glucose sensors in diabetes management: An updated review (2010-2020). *Chem. Soc. Rev.* **49**, 7671–7709 (2020).
38. L. Wang, S. Xie, Z. Wang, F. Liu, Y. Yang, C. Tang, X. Wu, P. Liu, Y. Li, H. Saiyin, S. Zheng, X. Sun, F. Xu, H. Yu, H. Peng, Functionalized helical fibre bundles of carbon nanotubes as electrochemical sensors for long-term in vivo monitoring of multiple disease biomarkers. *Nat. Biomed. Eng.* **4**, 159–171 (2020).
39. L.-C. Tai, W. Gao, M. Chao, M. Bariya, Q. P. Ngo, Z. Shahpar, H. Y. Y. Nyein, H. Park, J. Sun, Y. Jung, E. Wu, H. M. Fahad, D.-H. Lien, H. Ota, G. Cho, A. Javey, Methylxanthine drug monitoring with wearable sweat sensors. *Adv. Mater.* **30**, e1707442 (2018).
40. S. Lee, Y. J. Lee, J. H. Kim, G.-J. Lee, Electrochemical detection of H_2O_2 released from prostate cancer cells using Pt nanoparticle-decorated rGO–CNT nanocomposite-modified screen-printed carbon electrodes. *Chem* **8**, 63 (2020).
41. D. Ji, Z. Liu, L. Liu, S. S. Low, Y. Lu, X. Yu, L. Zhu, C. Li, Q. Liu, Smartphone-based integrated voltammetry system for simultaneous detection of ascorbic acid, dopamine, and uric acid with graphene and gold nanoparticles modified screen-printed electrodes. *Biosens. Bioelectron.* **119**, 55–62 (2018).
42. R. Jiménez-Pérez, J. González-Rodríguez, M.-I. González-Sánchez, B. Gómez-Monedero, E. Valero, Highly sensitive H_2O_2 sensor based on poly(azure A)-platinum nanoparticles deposited on activated screen printed carbon electrodes. *Sensors Actuat. B Chem.* **298**, 126878 (2019).
43. V. Vinoth, T. D. Shergilin, A. M. Asiri, J. J. Wu, S. Anandan, Facile synthesis of copper oxide microflowers for nonenzymatic glucose sensor applications. *Mat. Sci. Semicon. Proc.* **82**, 31–38 (2018).
44. B. Z. Chen, L. Q. Zhang, Y. Y. Xia, X. P. Zhang, X. D. Guo, A basal-bolus insulin regimen integrated microneedle patch for intraday postprandial glucose control. *Sci. Adv.* **6**, eaba7260 (2020).
45. J. Yu, Y. Zhang, Y. Ye, R. D. Santo, W. Sun, D. Ranson, F. S. Ligler, J. B. Buse, Z. Gu, Microneedle-array patches loaded with hypoxia-sensitive vesicles provide fast glucose-responsive insulin delivery. *Proc. Natl. Acad. Sci. U.S.A.* **112**, 8260–8265 (2015).
46. Z. Liu, J. Liu, T. Sun, D. Zeng, C. Yang, H. Wang, C. Yang, J. Guo, Q. Wu, H.-J. Chen, X. Xie, Integrated multiplex sensing bandage for in situ monitoring of early infected wounds. *ACS Sens* **6**, 3112–3124 (2021).
47. R. F. Donnelly, T. R. R. Singh, M. J. Garland, K. Migalska, R. Majithiya, C. M. McCrudden, P. L. Kole, T. M. T. Mahmood, H. O. McCarthy, A. D. Woolfson, Hydrogel-forming microneedle arrays for enhanced transdermal drug delivery. *Adv. Funct. Mater.* **22**, 4879–4890 (2012).
48. M. H. Ling, M. C. Chen, Dissolving polymer microneedle patches for rapid and efficient transdermal delivery of insulin to diabetic rats. *Acta Biomater.* **9**, 8952–8961 (2013).
49. C. P. Zhou, Y. L. Liu, H. L. Wang, P. X. Zhang, J. L. Zhang, Transdermal delivery of insulin using microneedle rollers in vivo. *Int. J. Pharm.* **392**, 127–133 (2010).
50. R. Schulz, K. Yamamoto, A. Klossek, R. Flesch, S. Hönzke, F. Rancan, A. Vogt, U. Blume-Peytavi, S. Hedtrich, M. Schäfer-Korting, E. Rühl, R. R. Netz, Data-based modeling of drug penetration relates human skin barrier function to the interplay of diffusivity and free-energy profiles. *Proc. Natl. Acad. Sci. U.S.A.* **114**, 3631–3636 (2017).
51. A. P. Raphael, S. C. Meliga, X. Chen, G. J. P. Fernando, C. Flaim, M. A. F. Kendall, Depth-resolved characterization of diffusion properties within and across minimally-perturbed skin layers. *J. Control. Release* **166**, 87–94 (2013).

Acknowledgments

Funding: The authors would like to acknowledge financial support from National Key R&D Program of China (grant nos. 2021YFF1200700 and 2021YFA0911100), the National Natural Science Foundation of China (grant nos. 32171399, and 32171456), the Guangdong Basic and Applied Basic Research Foundation (grant no. 2021A1515012261), the Fundamental Research Funds for the Central Universities, and Sun Yat-sen University (grant no. 22dfx02). L.J. would to thank the National Natural Science Foundation of China (grant no. 51975597) and the Natural Science Foundation of Guangdong Province (grant no. 2022B1515020011). **Author contributions:** X.X. conceived and designed the project. J.Y., L.J., and X.X. wrote the manuscript. X.X., L.J., H.-j.C., and J.W. guided the research, provided advice on this work, and edited the manuscript. J.Y. performed most of the experiments, analyzed the data, and completed the manuscript. S.Z. helped with data analysis, references, and graphics preparation. S.Z., D.M., and T.Z. developed the supporting circuit. X.H. and S.H. contributed to the in vivo experiments and the collection of data. All the authors discussed the results and commented on the manuscript. **Competing interests:** The authors declare that they have no competing interests. **Data and materials availability:** All data needed to evaluate the conclusions in the paper are present in the paper and/or the Supplementary Materials.

Submitted 22 February 2022
Accepted 8 November 2022
Published 14 December 2022
10.1126/sciadv.abo6900